MECHANORESPONSIVE BEHAVIORS OF ACTIN CYTOSKELETAL PROTEINS IN CELL SHAPE CHANGE PROCESSES

by
Eric S. Schiffhauer

A dissertation submitted to The Johns Hopkins University in conformity with the
requirements of the degree of Doctor of Philosophy

Baltimore, Maryland
October, 2018

ABSTRACT

For specialized cell function, as well as active cell behaviors like division, migration, and tissue development, cells must undergo dynamic changes in shape. To complete these processes, cells integrate chemical and mechanical signals to direct force production. At the core of cell shape change is the ability of the cell's machinery to sense mechanical forces and tune the force-generating machinery as needed. Force-sensitive cytoskeletal proteins, including myosin II motors and actin crosslinkers, such as alpha-actinin and filamin, accumulate in response to internally generated and externally imposed mechanical stresses, endowing the cell with the ability to discern and respond to mechanical cues. The physical theory behind how these proteins display mechanosensitive accumulation has allowed us to predict paralog-specific behaviors of different crosslinking proteins and identify a zone of optimal actin-binding affinity that allows for mechanical stress-induced protein accumulation. It also allowed us to uncover a regulatory mechanism that utilizes the biphasic nature of mechanoresponse to tune the myosin II mechanoresponsiveness in mammalian cells. These molecular mechanisms coupled to the mechanical feedback systems ensure robust shape change, but if they go awry, they are poised to promote disease states, such as cancer cell metastasis and loss of tissue integrity.

Faculty Sponsor: Douglas N. Robinson, Ph.D., Professor of Cell Biology

Reader: Erin Goley, Ph.D., Associate Professor of Biological Chemistry

ACKNOWLEDGEMENTS

First, I would like to acknowledge my advisor, Doug, for his excellent mentorship. Since before I started in the Robinson laboratory, Doug built an environment of open discussion without any barriers to topics discussed, ideas for the future of our science, or criticisms of current thinking. He also has shown the ability to adapt his mentorship style to the individual student: he provides students with only as much oversight as he believes they need. Doug's eagerness to provide close training in my first few years, followed by the space to test my own ideas and design my own experiments in the final few years allowed me the room to grow into an independent thinker. He also taught me to be my own toughest critic, that it is better to face the toughest scrutiny at home than from outsiders, and that with enough preparation the tasks that seem difficult can become simple and easy. He provided me with the opportunity to be exposed to science from around the world and to meet the leaders of my field by sending me to national conferences on more than an annual basis, which allows me to now speak with confidence and to converse with experts comfortably. I would also like to thank my lab mates, especially Hoku, Alexandra, Vasudha, Cathy, Tianzhi, Priyanka, Corinne, Dustin, Jenny, Yinan, Shantel, Brian, Ly, Kat, Eleana and Laura. You all made me a better scientist and a better person by pushing my ideas and testing my assumptions. More importantly, you all made the lab a fun place to be, and when everyone is having fun, I believe the best work gets done. I will miss our lab meetings and our lunch conversations, and I will probably not be as familiar with the music played on the radio ever again. Thanks also to my fellow BCMB classmates, who made the especially the first two years of the program some of the best I have had in my life. You all made the courses easier and the weekends much harder to say goodbye to. I am not sure I would have made it through oral examinations without your support.

I also would like to thank my parents for their guidance for my entire life, but especially for the last few years. My mother taught me to have a passion for science from the time I was young, by showing me physiology text books and teaching me to read ECGs. My father is one of the hardest-working people I have ever met; he taught me to how to persevere even when the love for the task began to run out. I want to thank my sister, Rachel, for her caring support and for smoothing the path for me as the first in our family to go to college and graduate school. Last, but not least, I would like to thank my wife, Maggie. You have spent so much patience on me in the past four years, and you have magnified my happy moments and shared the burden of my harder ones. You have believed me capable of more than I believe myself and helped me to strive for the best of my ability.

TABLE OF CONTENTS

Abstract……………………………………………………………………………………..ii

Acknowledgements…………………………………………………...………..……..iv

Chapter 1: Introduction…………………………………………………..…………1

Chapter 2: Mechanoaccumulative elements of the mammalian actin cytoskeleton……………………………………………………………………………15

Identification of mechanosensitive cytoskeletal elements……...……………15

Non-muscle myosin II mechanosensation……………………...………….18

Paralog-specific mechanoresponsiveness of actin crosslinking proteins..22

Paralog-specific mechanoresponsiveness of α-actinin ..…………………....23

Paralog-specific mechanoresponsiveness of filamin………..……………….29

Conclusions……………………...………………………………………………31

Chapter 3: PKCζ provides setpoint control for myosin IIB mechanosensitive dynamics………………………………………………………………………………32

Myosin II heavy chain phosphorylation controls mechanoresponse in *Dictyostelium* in a biphasic manner………………..………………………….34

NMIIB cytoskeletal enrichment predicts mechanoresponsiveness in mammalian cells in a biphasic manner……………………..………………….36

NMIIB heavy chain phosphomimetic and non-phosphorylatable mutants change cortical enrichment and mechanoresponsiveness………………..…39

PKCζ expression and activity alters NMIIB cortical association and mechanoresponsiveness………………………...……..……………………..….42

NMIIB mechanoresponsiveness depends on the fraction of free and assembled myosin II, not concentration of monomers………..……….…..45

Chapter 4: Conclusions……………………………………………………………...…49

Chapter 5: Future directions…………………………………………………………..………52

Chapter 6: Materials and methods…………………………………………………………56

Contributions…………………………………………..……………………….....……66

Bibliography……………………………………………….………………………….67

Curriculum Vitae……………………………………………………………….......……76

LIST OF FIGURES

Figure 1.1: The structure of the cortex dertermines its physical properties……..…2

Figure 1.2: Integrated chemical and mechanical feedback loops drive cleavage furrow ingression…………………………………………………………..….8

Figure 1.3: Mechanoaccumulation by actin-binding proteins is determined by an optimal zone of actin-binding affinity…………………………………………..……10

Figure 2.1: Five actin-binding proteins respond to an externally applied mechanical stress..……….……………………………………………….…..…15

Figure 2.2: Actin-binding proteins respond most-strongly to externally applied Stress…………………………………………………………………………..…16

Figure 2.3: Myosin IIB mechanoresponse is not dependent on endogenous Expression or myosin IIA mechanoresponse…………………………..……19

Figure 2.4: Myosin IIA and IIC show mechanoaccumulation in all contexts examined, whereas myosin IIB shows mechanoaccumulation in distinct cell types and phases of the cell cycle……...……………………………..…….21

Figure 2.5: A force-dependent model based on actin binding affinity predicts the mechanoaccumulative behavior of α-actinins, and the high affinity α actinin-4 mutant K255E is non-mechanoresponsive………….………………23

Figure 2.6: Mechanoresponsiveness of myosin II and anillin in HeLa cells...……..25

Figure 2.7: Modeling and measuring the mechanisms of filamin and α-actinin mechanoresponse…………………………………………………………………27

Figure 2.8: A force-dependent model based on actin binding affinity predicts The mechanoaccumulative behavior of filamin to a region of shear deformation, followed by myosin-driven cell tip accumulation……………..28

Figure 3.1: Myosin II cytoskeletal association and mechanoresponsiveness have a biphasic relationship in *Dictyostelium*…………………..……..……………34

Figure 3.2: Myosin IIB cytoskeletal enrichment predicts mechanoresponsiveness In mammalian cells in a biphasic manner…………………………………………36

Figure 3.3 Magnitude of mechanoresponse is independent of intensity of GFP-NMIIB in cells………………………………………………………………38

Figure 3.4. Myosin IIB heavy chain phosphomimetic and non-phosphorylatable mutants change cortical enrichment and mechanoresponsiveness………39

Figure 3.5. PKCζ expression and activity alters NMIIB cortical association and mechanoresponse………………………………………………………………42

Figure 3.6. PKCζ overexpression and NMIIA knockdown alter mechanoresponse in HeLa cells………………………………………………………………………43

Figure 3.7. Concentration of monomeric NMIIB in cells does not predict mechanoresponse………………………………………………………………44

Figure 3.8. Relationship between NMIIB mechanoresponsiveness and cytoskeletal association is biphasic…………………………………………………………45

CHAPTER 1. INTRODUCTION

The concept “form begets function begets form” provides an excellent foundation for understanding the behavior of biological systems. Even cells, the smallest unit of complex living systems, assume distinct shapes, mechanical properties, and physical behaviors to perform all of the necessary functions of an organism. Different cell types use a common set of cytoskeletal elements to provide precise physical support for their distinct functions. For example, red blood cells and neurons have very different shapes that allow them to perform their specific roles. However, they both utilize alternating patterns of actin and spectrin to form cortices with appropriate viscous and elastic properties, albeit in different structural arrangements. Perturbations to this structural network cause a breakdown in the mechanical properties, or the “form”, of these cells, which inhibits cell function (1, 2).

Fascinatingly, the physical properties of cells are both determined and acted upon by the cytoskeletal apparatus. Cells are capable of modifying their own physical properties and driving changes in cell shape in response to internal and external chemical and mechanical stimuli. These modifications occur through the remodeling of the cell cortex, the network of cytoskeletal proteins directly under the plasma membrane. Much progress has been made recently in deciphering how chemical signals drive mechanical changes, as well as how internally- and externally-generated mechanical cues modulate chemical signaling in the cell. A more complete mechanistic understanding of the interface between mechanical and chemical signals that drive cell behavior, including tissue development and cancer metastasis, will be needed to modulate these systems for the treatment of developmental and metastatic diseases.

Force generation by, and active remodeling of, the cytoskeletal network at the cortex primarily drive cell shape change. The cortex contains structural proteins each with distinct physical properties and kinetics of binding and detachment that are poised to

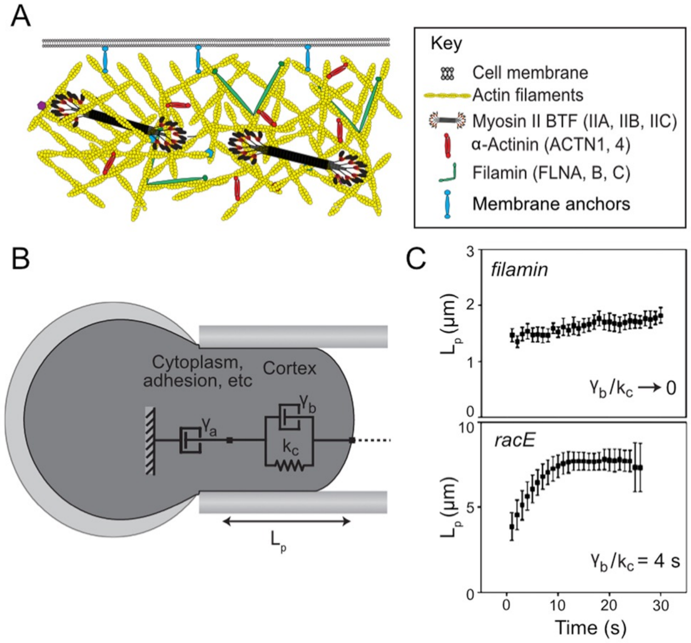
A
Key
Cell membrane
Actin filaments
Myosin II BTF (IIA, IIB, IIC)
α-Actinin (ACTN1, 4)
Filamin (FLNA, B, C)
Membrane anchors
B
Cytoplasm, adhesion, etc
Cortex
γ_a
γ_b
k_c
L_p
C
filamin
L_p (μm)
$\gamma_b/k_c \rightarrow 0$
racE
$\gamma_b/k_c = 4$ s
0
1
2
3
5
10
0
10
20
30
Time (s)

Fig. 1.1. The structure of the cortex determines its physical properties. (**A**) Major components of the actin cytoskeleton in the cell cortex shown roughly to scale for mammalian cells. (**B**) A simple model of cell mechanics, where the spring k_c and the viscous damper γ_b describe the elastic and viscous contributions by the cortex, respectively. The damper γ_a primarily describes the viscous contribution by the cytoplasm. Upon aspiration of *Dictyostelium* cells into a micropipette using a fixed pressure, the length of the cell protruding into the pipette (L_p) is observed over time. The model in (**B**) can be accurately used to describe the "creep" of the cells into the pipette in (**C**). The slope of the first and second phases of deformation can be used to compute the value of the viscous dampers and γ_a, respectively. The amplitude of the initial length deformation can be used to determine the elastic parameter k_c. In the *filamin*-null*,* the contribution of initial damper γ_b is much smaller than that of k_c, and so initial deformation happens in less than one second. The continued flow can be described by γ_a. In the *racE*-null, the contribution by γ_b is quite large, causing slow initial deformation, while γ_a is quite small, displaying no creep in the second phase of deformation.

respond dynamically to chemical and mechanical signals to effect shape change. The cortex is comprised of actin filaments organized in a meshwork ~200-nm thick (3, 4), crosslinked by actin-crosslinking proteins and non-muscle myosin IIs, which are the primary drivers of network contraction in cells. Among these structural elements are regulatory proteins that control actin and myosin dynamics, factors regulating protein turnover, membrane linkers, scaffolding/adaptor proteins, Rho GTPases, Rho GTPase effectors, and Rho GAPs/GEFs (5). The actin filaments in the cortex are quite short: in the social amoeba *Dictyostelium discoideum*, the average actin filament length is ~100 nm (4, 6). In mammalian cells, identifying a characteristic length is more challenging because of cell-type diversity, but for leukocytes the majority of filament are <180 nm in length (7), slightly longer than in *Dictyostelium.* Crosslinkers anchor these filaments to one another to create the actin meshwork. Crosslinker lengths vary considerably. For example, α-actinin, which binds actin filaments in parallel or anti-parallel orientation, is around 35 nm in length (8), while filamin is 160-190 nm (9). To actively contract the actin-network, myosin II monomers (a functional monomer includes two heavy chains, two essential and two regulatory light chains) assemble into functional bipolar filaments, which are ~300 nm in length (10). Thus, actin filaments do not dominate the scale of the cortex by length, rather each of these components are of similar scale (**Figure 1.1A**). In the same way, the mechanical properties of the cortex are not dominated entirely by the properties of actin filaments, but by this dynamic network of structural and regulatory proteins.

Mechanically, the cell cortex can be described as viscoelastic, or having both elastic and viscous characteristics. When probed using very small deformations, such as those imposed by laser-tracking microrheology, the cytoskeleton can be described as having power-law mechanics with the characteristics of a soft glassy material. Elasticity in the material comes from cytoskeletal elements maintaining relatively fixed relationships to one another due to the actin crosslinkers and network entanglements that holds the filament network together. Viscosity, however, requires the ability of these connections from crosslinkers and entanglements to release so that the cytoskeletal elements can rearrange. Furthermore, in cells, active processes that require ATP hydrolysis can also ‘stir’ these elements, promoting the emergence of a viscous-like character (11, 12). Cell-cortex mechanics at these scales have been analyzed in *Dictyostelium* (4, 13, 14) and in multiple mammalian cell types (15, 16). On these low-force regimes, cells are predominantly elastic with a mechanical phase angle of ~10-15°. Further, cells indeed show power-law mechanics over multiple logs of time scale (from sub-ms to 100s of ms).

However, on longer time-scales, active processes in *Dictyostelium* begin to dominate these low force-regime mechanics (14).

Cell mechanics at larger force regimes and larger deformations, such as cytokinesis or those imposed by micropipette aspiration, can be described phenomenologically by simpler mechanical models that incorporate elastic springs and viscous dampers (dashpots) (**Figure 1.1B**). In one arrangement, the so-called Voigt model, a viscous damper (γ_b, nN•s/μm^3) is placed in parallel with an elastic spring (k_c, nN/μm^3) to approximate the cytoskeleton. In addition, many shape change processes are damped by the viscosity contributed by long time-scale cortex remodeling and the cytoplasm, which can be modeled by incorporating an additional viscous damper, γ_a, placed in series (**Figure 1.1B**)(17). Upon the application of a fixed pressure by micropipette aspiration, the cell will deform into the pipette a length, L_p (**Figure 1.1B**)(17). In wild-type and *filamin*-null *Dictyostelium,* damper γ_b approaches zero, so the initial deformation is largely elastic and happens in less than one second (**Figure 1C**)(18). However, in some mutants where cytoskeletal regulation is disturbed, such as in the *racE*-null *Dictyostelium*, the damper γ_b becomes significant, and the initial deformation occurs over a few seconds (**Figure 1.1C**)(18). When parameterized with directly measured values, these models help account for cell behavior during retraction from an applied force (18), cytokinesis (19, 20), and cell motility (17, 21).

Forces acting on the cell cortex

The forces acting on the cell cortex during shape change processes can be divided into inward and outward forces, where inward forces pull the cortex toward the cell center and outward forces push the cortex away from the cell center. Inward forces include Laplace pressure, contraction driven by myosin motors, and actin crosslinker dynamics coupled with actin polymer disassembly (18-20, 22). An ideal process for studying these inward forces is cytokinesis, where cells must contract inward along the cleavage furrow to divide one cell into two. During *normal* cell division of almost all eukaryotic cell types, non-muscle myosin II accumulates at the equatorial region of the cell in response to signals from the mitotic spindle, where it contracts the actin-network to drive furrow ingression. However, in many cell types (*Dictyostelium*, yeast, and mammalian cells), cells are capable of dividing without myosin II. How is this possible? From studies of *myosin II*-null *Dictyostelium* dividing on surfaces, the major driving force for furrow ingression is actually the Laplace pressure (4). Laplace pressure results from the pressure difference (ΔP) between the inside (P_{in}) and outside (P_{out}) of a liquid interface, and is proportional to the product of the surface (cortical) tension and local curvature ($\propto$ radius^{-1}) of the fluid surface (19). Because of Laplace pressure, mitotic *Dictyostelium* cells can divide by traction-mediated cytofission, where adherent cells protrude in two directions, making division across the long axis energetically favorable. The initial increase in curvature in the furrow region upon cell elongation combined with cortical tension leads to increased inward stresses, promoting furrow ingression. Then, as the furrow ingresses, the surface curvature increases, leading to a positive feedback (19). Other types of myosins also contribute to cytokinesis and can do so by impacting these cell mechanics. For example, by providing membrane-cortex linkages, myosin I motors contribute significantly to cortical tension (23). Myosin II-independent cytokinesis is not restricted to *Dictyostelium,* and likely explains how mammalian cells can divide with myosin II inhibition if the adhesion conditions are appropriate (24), and in tissues when the myosin II-actin-bound state is prolonged to last an entire cytokinesis furrow ingression event (25).

In fact, in *Dictyostelium,* normal myosin II activity leads to a slowing down of furrow ingression during late stages of cytokinesis (20). Wild-type *Dictyostelium* cells are more deformable in the polar cortex than at the furrow, while there is limited mechanical differential in the *myosin II*-null cells (4). This differential leads to two consequences of cell mechanics that likely contribute to this slowdown of furrow ingression in wild-type cells (19, 20). First, as the furrow ingresses, resistive stresses can build in the two daughter cell cortices and cytoplasm, slowing furrow ingression. Genetic mutants devoid of myosin II, key actin crosslinkers, or cytoskeletal regulators that control the polar cortices appear to alleviate this resistive stress (4). Second, the accumulation of the cytokinetic machinery, including myosin II and actin-crosslinkers, to the cleavage furrow cortex can lead to strain-stiffening of the cytoskeletal network, making it more difficult for the cortex network to remodel (making it more elastic) (19, 22). Most likely, both properties (resistive stresses and strain-stiffening) contribute to the wild-type furrow ingression dynamics.

To drive outward force generation, cells primarily use actin-assembly and/or pressure-induced blebs. An ideal cellular process for studying the generation of outward forces is the leading edge of a migrating cell. At this edge, the forward-driving force is either driven by the well-defined Arp2/3 Brownian ratchet (26-28), or pressure-induced bleb formation by myosin activity in highly confined, compressed environments (29, 30). The Arp2/3 Brownian ratchet moves the plasma membrane forward by stimulating the creation of many new actin filament branches at the leading edge. Thermal fluctuations in each of these filaments creates space for actin monomers to be added to the barbed end of the growing filament, driving the membrane forward (26-28). In another type of motility, termed lobopodial migration, cells in confined environments pull their nuclei forward by myosin II contraction, using the nucleus as a piston to create enough pressure to drive bleb formation at the cell front (31). These blebs then rapidly fill with actin-cytoskeletal components, creating a new cortex (29, 30). In both cases, the process that allows faster membrane protrusion should determine the dominant behavior.

Chemical and mechanical inputs direct shape change

During cell shape change behaviors, including cytokinesis and cell migration, two distinct classes of contributions control the direction, magnitude, and robustness of the process: chemical and mechanical inputs. An example of a chemical input is the external chemical gradient of cAMP sensed by *Dictyostelium* during chemotaxis (32), which drives the directional activation of the branched actin network in pseudopods at the cell front and the contraction of myosin II at the cell back. Chemical signals can also be internal, such as those from the mitotic-spindle-associated chromosomal passenger complex proteins (CPCs) INCENP (inner centromere protein) and kinesin 6, which promote cytokinesis (33, 34). However, the spindle is not essential for symmetrical or asymmetrical cytokinesis in many cell types (35-38). In reality, the integration of both chemical and mechanical signaling drives cytokinesis (**Figure 1.2**). In *Dictyostelium,* myosin II and cortexillin I, an actin crosslinker, initially accumulate to the cleavage furrow as a result of spindle signaling. However, when mechanical stress is applied to the cortex, the existing myosin II bipolar filaments experience this stress, which leads to a local increase in myosin II concentration. In the context of cytokinesis, this cooperative myosin II assembly occurs even in the absence of spindle-associated chemical-signaling inputs (39-41). Molecularly, under resistive load, the myosin II lever arms stall in the phase of the power stroke that is the isometric, cooperative binding state. First, the myosin II duty ratio is load-sensitive. In mammalian nonmuscle myosin IIB, for example, when a myosin II head imposes a piconewton-range resistive load on another, the second head releases ADP at a 10-fold slower rate than an unloaded head ($0.023\pm0.003 s^{-1}$ versus $0.27\pm0.06 s^{-1}$) (42). Second, more than just inhibiting ADP-release, force can trap the myosin II motor in the cooperative isometric state, which promotes the binding of additional myosin motors to the actin filament nearby due to a propagated conformational change in the actin filament (43-45). This cooperative binding state was specifically implicated in mechanosensitive accumulation by experiments where the myosin II lever arm was lengthened or shortened (40). A longer lever arm led to greater accumulation at lower applied stresses while shortening the lever arm led to significantly reduced accumulation across all pressure ranges. Additional controls ruled out myosin II motility velocity as the explanation. This cooperative accumulation can account quantitatively for myosin and cortexillin I accumulation in response to mechanical stress (41). Further, this cooperative accumulation can account for the insertion of myosin II into the cortex of the cleavage furrow, where it promotes additional accumulation of kinesin 6 (Kif12) and INCENP through the cortexillin I-binding IQGAP2 (GapA) (46) (**Figure 1.2**). Thus, the cleavage furrow cortex comprises a mechanochemical feedback loop, where both chemical and mechanical signals promote accumulation of the appropriate machinery (46, 47). This system is inherently quite robust; the network of cytokinesis cytoskeletal machinery stabilizes under mechanical load in a manner that is independent of any single protein (22).

Another interesting example of mechanical and chemical signaling integration that drive cell shape change can be found in cell-surface proteins that associate between cells. During myoblast fusion in *Drosophila*, the cell-surface markers Sns and Duf of the fusion-competent cell and founder cell, respectively, associate to activate downstream signaling in both cells (39). In the fusion-competent cell, Sns signaling activates WASP to drive the assembly of an actin focus, which pushes finger-like actin projections into the founder cell. In the founder cell, signaling downstream of Duf drives Rho activation and myosin II contractility, allowing the cell to oppose the projections with enough force to allow cell-cell fusion (39). Interestingly, in the absence of the cytoplasmic domain of Duf, myosin II still accumulates at the site of cell-cell fusion in the founder cell. This accumulation appears to be due to the same force-dependent assembly of myosin II into bipolar filaments (39).

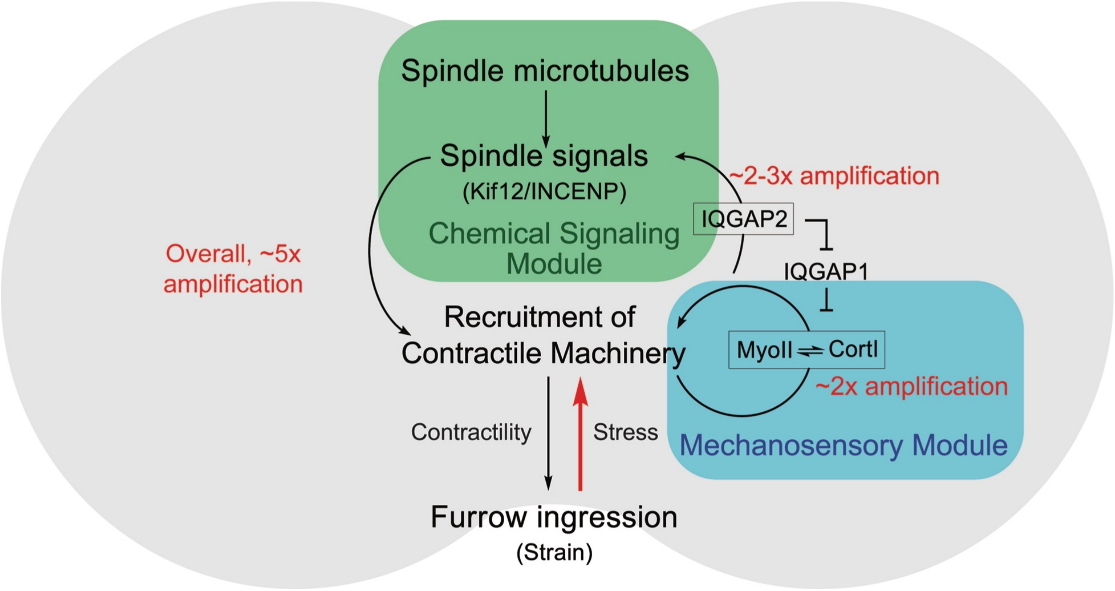
Spindle microtubules
Spindle signals
(Kif12/INCENP)
Chemical Signaling Module
~2-3x amplification
IQGAP2
IQGAP1
Overall, ~5x amplification
Recruitment of Contractile Machinery
MyoII ⇌ CortI
~2x amplification
Contractility
Stress
Mechanosensory Module
Furrow ingression
(Strain)

Fig. 1.2. Integrated chemical and mechanical feedback loops drive cleavage furrow ingression. At the cleavage furrow of dividing *Dictyostelium*, the Chemical Signaling Module, including INCENP and Kif12 (the kinesin 6 family protein), can activate the recruitment of contractile machinery, including cortexillin I (CortI) and myosin II (MyoII). Simultaneously, the contractile machinery, which comprises the Mechanosensory Module, can accumulate in response to the forces created by furrow ingression and drive the activation of the chemical signaling module through IQGAP2. The overall system allows for ~5-fold amplification of myosin II accumulation at the cleavage furrow in response to mechanical stress.

Force-sensing by other actin-associated proteins

A number of other actin-binding proteins have demonstrated the ability to sense and respond to force. In the adherens junctions of epithelial cells, the minimal cadherin-catenin complex, including α-catenin, β-catenin, and E-cadherin, interacts with actin-filaments in a force-dependent manner. Force propagating from the actin cytoskeleton of one cell to another through E-cadherin attachments increases the binding lifetime of the cadherin-catenin complex to actin. In single molecule experiments, the complex-actin binding lifetime increases from ~60 ms at low force to ~120 ms at 10 pN of applied force (48). At higher forces, these bonds then slip so that they display a catch-slip behavior, depending on the force-regime. The catch-slip bond's contribution to the mechanosensitive accumulation (the accumulation of a protein in response to applied stress) of the actin crosslinking protein α-actinin and filamin have been demonstrated in *Dictyostelium* (18, 49). The mechanosensitive accumulation of mammalian α-actinin and filamin paralogs will be covered in detail in Chapter 2. Briefly, mechanoaccumulation is unique to the α-actinin 4 paralog, and is not observed for α-actinin 1 (**Figure 1.3A**) (18, 49), and is likely important for its recruitment to focal adhesions under high tension (50). Similarly, the mammalian paralog filamin B shows higher mechanosensitive accumulation than filamin A (**Figure 1.3B**). In both cases, reaction-diffusion models (**Figure 1.3C,D**) for force-dependent binding can predict which paralog will accumulate based on the intrinsic difference in actin-binding affinity of the paralogs (49)**.** The models

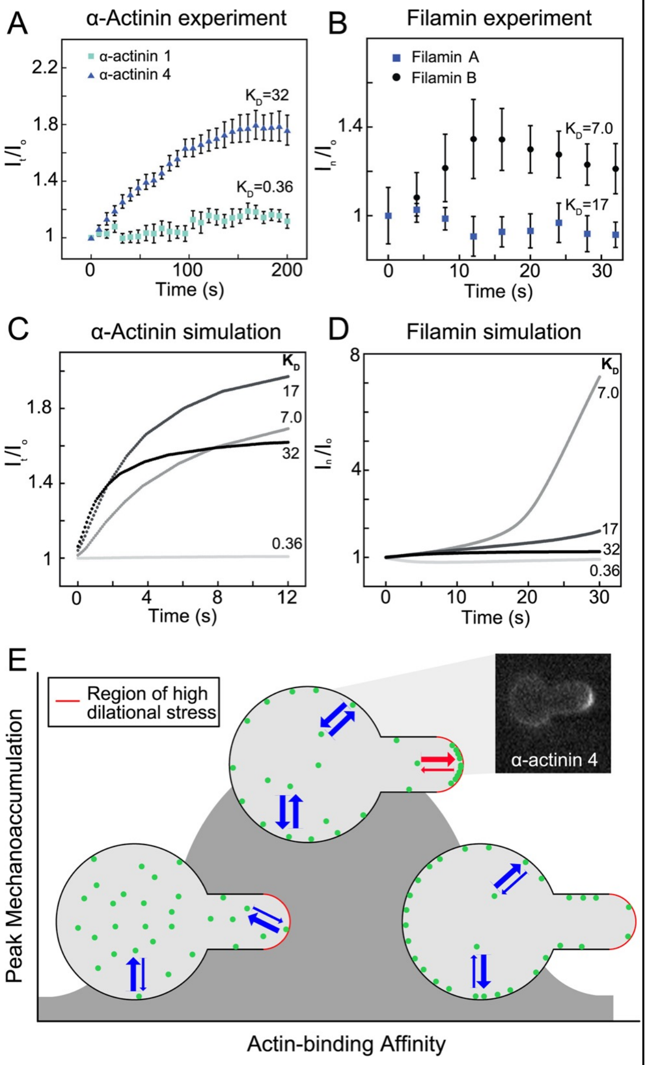

Fig. 1.3. Mechanoaccumulation by actin-binding proteins is determined by an optimal zone of actin-binding affinity (**A**) The low-affinity α-actinin 4, transfected into HeLa cells, accumulates over time in response to micropipette aspiration at a region of high network dilation, the "tip" of the cell (calculated by fluorescence intensity at the tip, I_t, normalized to the fluorescence intensity at the opposite side of the cell, I_o). The high-affinity α-actinin 1 does not accumulate. (**B**) The high-affinity filamin B accumulates to a region of high shear deformation, the "neck" of the cell, during micropipette aspiration (calculated by the fluorescence intensity at the neck, I_n, normalized to the fluorescence intensity at the opposite side of the cell, I_o). The lower affinity filamin A does not accumulate. For filamin B, a second phase of myosin II-mediated flow carries the protein to the tip, which accounts for the decrease beginning around 12 s. (**C**) The accumulation of a force-dependent actin-binding protein like α-actinin is modeled using four different actin-binding affinities, using a reaction-diffusion model of force-dependent actin binding using physiological G- and F-actin concentrations, crosslinker concentrations, and published actin binding affinities. (**D**) The accumulation of filamin is modeled using the same four actin-binding affinities but considering cooperativity to account for the accelerating rate of accumulation. The results show that an optimal dissociation equilibrium constant (K_D) to actin exists for both non-cooperative (α-actinin) and cooperative (filamin) actin-binding proteins where mechanoaccumulation is maximized. Please note that for panels C and D, the affinities represent the affinities of single actin binding heads, and not an overall apparent affinity from the complete crosslinking reaction. (**E**) At a high actin-binding affinity, actin crosslinking proteins do not have a large enough unbound pool to dynamically respond to force applied during micropipette aspiration. At a very low actin-binding affinity, actin-binding proteins do not bind the cortex with enough affinity to remain locked-on at sites of mechanical stress. Thus, an optimal zone exists for actin-binding affinity where mechanoaccumulation is maximal. This is demonstrated by the inset, showing accumulation of α-actinin 4 during micropipette aspiration.

utilize parameters for crosslinker concentration, diffusion rates, on- and off-rates for actin binding measured in *Dictyostelium* and mammalian cells, and the catch-slip characteristics of the bonds (18, 49, 51). The models recapitulate the kinetics of protein accumulation over time, capturing a sigmoidal rise for filamin, and an exponential rise for α-actinin. The models also illuminate an optimal actin-binding affinity zone for mechanoresponsive proteins. In other words, if the intrinsic actin-binding affinity of a crosslinker is too high, the cell will not have a sufficient monomeric pool available to respond to the applied force, and if the affinity is too low, the protein will not bind actin well enough to stay bound to the network in regions of stress (**Figure 1.3E**). The exact set-point where the actin-binding affinity is ideal for mechanoresponse also depends on cooperativity: a model that invokes cooperative actin-binding predicts a lower set-point than one without cooperativity. The cooperativity in the model used to predict filamin accumulation is the reason the filamin model predicts a lower ideal actin affinity for mechanoaccumulation than the α-actinin model does (49) (**Figure 1.3C,D**).

The branched actin network itself also responds to mechanical inputs, affecting cell shape change. The forced curvature of actin filaments beyond normal fluctuations in actin filament bending promotes the binding of the Arp2/3 complex to the convex side of the filament (52). This can explain how actin filaments bent along the front edge of a migrating cell ensure the binding of the Arp2/3 complex to the convex side, allowing branching of a new filament in the direction of the plasma membrane. Similarly, the application of load to branched actin networks as they assemble drives an increase in the density and number of actin filaments, through the formation of up to 3.5-fold more Arp2/3 complex-mediated actin branches and 3-fold tighter actin filament packing, while not changing the length of the filaments (53). This ability to build variably-dense actin networks provides cells the adaptability to push their leading edge through extracellular environments of variable stiffness.

Mechanochemical signaling allows dynamic escalation of force-production

To accomplish the fundamental processes involving cell-shape change, cells integrate chemical and mechanical inputs and ensure robust completion of the task with remarkable versatility. During cytokinesis, *Dictyostelium* myosin II is likely capable of a 30-50-fold dynamic range in force production, through a 3-5 fold increase from accumulation of myosin II at the furrow by chemical and mechanical signals (46) and a 5-8 fold increase in duty ratio under applied load. This 5-8 fold increase due to a shift in duty ratio assumes that *Dictyostelium* myosin II shows a similar force-dependent duty ratio as observed for mammalian nonmuscle myosin II (42) (**Figure 1.2**). Even this dynamic range underestimates the cell's capabilities, because without myosin II, the cells can divide using Laplace pressure, which can be an order of magnitude more powerful than myosin II-mediated contractility (19, 20). Similarly, cells can theoretically increase the "motor output" of the Arp2/3 complex-actin network at the leading edge by an order of magnitude during migration by force opposition alone (53).

The relative expression of mechanosensory proteins provides yet another level of control by cells. By expressing mechanoresponsive isoforms of myosin II, α-actinin, or filamin, a mammalian cell can tune its ability to rapidly respond to imposed force. In fact, the mechanoresponsive crosslinker α-actinin 4 is essential for pancreatic cancer cell migration, was increased in expression in 63% of pancreatic cancer patients, and was a significant negative predictor of patient survival (54). Thus, understanding how and which proteins are essential for mechanical stress-response may provide new strategies for stopping the force-dependent processes essential to cancer cells, such as division, migration, and metastasis.

In addition, it will be important to delve deeper into the integration of chemical and mechanical signals in cells. For example, chemical signaling from Rac1 is known to activate PKC, which contributes to mammalian myosin light chain and heavy chain phosphorylation (55, 56). PKC's phosphorylation of the Myosin IIA heavy chain at S1916 is essential for the cell's ability to sense and respond to the mechanical input of substrate stiffness at focal adhesions (57). In Chapter 2, we demonstrate that Myosin IIB shows differential mechanoresponsiveness across cell types, and within a cell-type, myosin IIB shows differential mechanoaccumulation across the phases of the cell cycle (49). As myosin IIB's subcellular localization is regulated primarily by a single site of heavy chain phosphorylation (58), the tuning of this myosin's mechanoaccumulative ability by heavy chain phosphorylation will be investigated in Chapter 3.

In addition, skeletal muscle myosin II has mechanical compliance in the tail region that can be even larger than the head region (59). Thus, mechanical strain across the myosin filaments could provide a basis for cross-talk between the motors and tails under mechanical load. Compliance in the non-muscle myosin II tail has not yet been definitively demonstrated. However, the ability of a long lever arm mutant myosin (2xELC) in the context of the phosphomimic (3xAsp) tail mutant to assemble into filaments *in vivo* is highly consistent with the concept of cross talk between the two parts of the myosin molecule (60). Also, molecular simulations accurately depicting the behavior of non-muscle myosin II in response to an applied stress require not just force feedback, but strained and unstrained states of myosin II bipolar filaments, wherein the strained state the myosin remains assembled until the bipolar filament relaxes (47). Thus, an important concept to be tested for non-muscle myosin II is whether there is compliance in the non-muscle myosin II tail, and how this compliance affects its mechanosensitive assembly and phosphoregulation. These answers will be essential for learning how to tune the cellular response to the mechanochemical inputs that drive cell-shape change processes in normal and disease states.

CHAPTER 2. MECHANOACCUMULATIVE ELEMENTS OF THE MAMMALIAN ACTIN CYTOSKELETON

As mentioned above, to change shape, divide, form junctions, and migrate, cells reorganize their cytoskeletons in response to changing mechanical environments (61-64). Actin cytoskeletal elements, including myosin II motors and actin crosslinkers, structurally remodel and activate signaling pathways in response to imposed stresses (46, 65-68). Recent studies demonstrate the importance of force-dependent structural rearrangement of α-catenin in adherens junctions (48) and vinculin's molecular clutch mechanism in focal adhesions (69). However, the complete landscape of cytoskeletal mechanoresponsive proteins and the mechanisms by which these elements sense and respond to force remain to be elucidated. To find mechanosensitive elements in mammalian cells, we examined protein relocalization in response to controlled external stresses applied to individual cells. Here, we show that non-muscle myosin II, α-actinin, and filamin accumulate to mechanically stressed regions in cells from diverse lineages. Using reaction-diffusion models for force-sensitive binding, we successfully predicted which mammalian α-actinin and filamin paralogs would be mechanoaccumulative. Furthermore, a Goldilocks zone must exist for each protein where the actin-binding affinity must be optimal for accumulation. In addition, we leveraged genetic mutants to gain a molecular understanding of the mechanisms of α-actinin and filamin catch-bonding behavior. Two distinct modes of mechanoaccumulation can be observed: a fast, diffusion-based accumulation and a slower, myosin II-dependent cortical flow phase that acts on proteins with specific binding lifetimes. Finally, we uncovered cell-type and cell-cycle-stage-specific control of the mechanosensation of myosin IIB, but not myosin IIA or IIC. Overall, these mechanoaccumulative mechanisms drive the cell's response to physical perturbation during proper tissue development and disease.

Identification of mechanosensitive cytoskeletal elements

To identify mechanosensitive elements, we examined protein relocalization in response to controlled external stresses applied locally to individual cells. We characterized more than 20 actin-binding, signaling, and lipid-binding proteins by transiently expressing fluorescently-tagged constructs in Jurkat T-cells (**Fig. 2.1**), NIH 3T3 fibroblasts (**Fig. 2.2A**), HeLas (**Fig. 2.2B**), and HEK 293Ts (**Fig. 2.2C**). Cells were deformed into the pipette by micropipette aspiration (MPA) (70) to a length twice the radius of the pipette ($2L_p/R_p$) for five minutes using a fixed pressure defined by their mechanical properties (Jurkat: 0.075 nN/μm^2; NIH 3T3: 0.15 nN/μm^2; HEK 293T: 0.15 nN/μm^2; HeLa: 0.2 nN/μm^2). We have previously determined computationally that the tip region in the pipette is the region of highest dilational deformation, while the pipette neck experiences shear deformation (18). The concept of dilation of the cytoskeleton at the tip region is

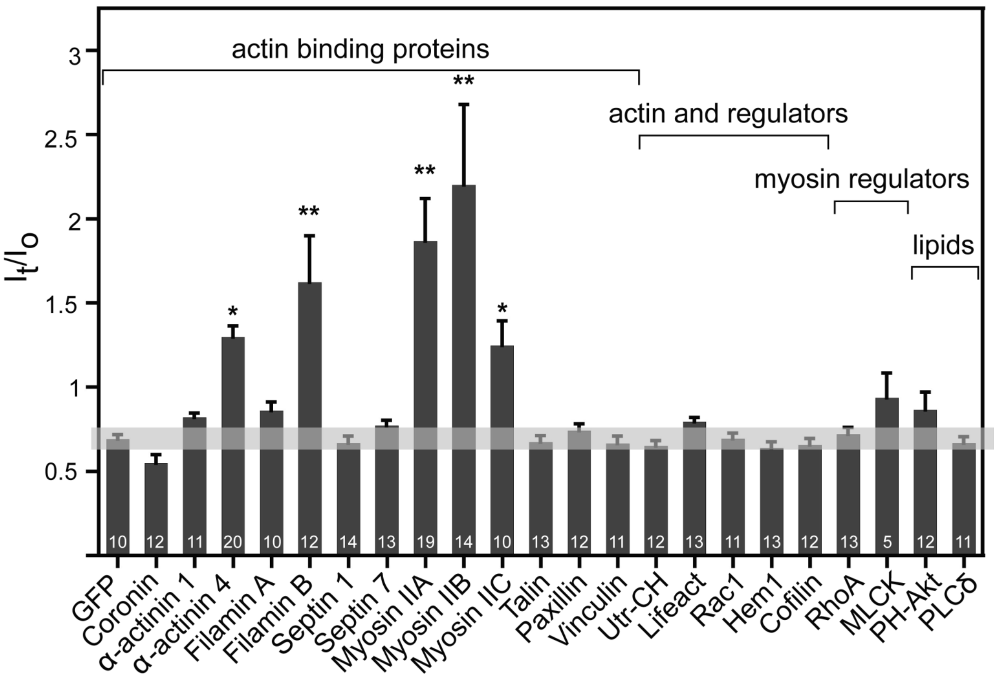

Fig. 2.1. **Five actin-binding proteins respond to an externally applied mechanical stress.** A ratio (I_t/I_o) of maximum tip intensity (I_t) to opposite cortex intensity (I_o) shows that actin-binding proteins α-actinin 4, filamin B, myosin IIA, myosin IIB, and myosin IIC accumulated to the highest level among 22 cytoskeletal, signaling, and lipid-binding proteins in Jurkat cells (*p<0.05, **p<0.0001).

also supported by the immediate decrease in actin density upon deformation by MPA (not shown), similar to what has been observed in red blood cells (71). Furthermore, although the actin network has a very fast recovery time, a significant immobile fraction

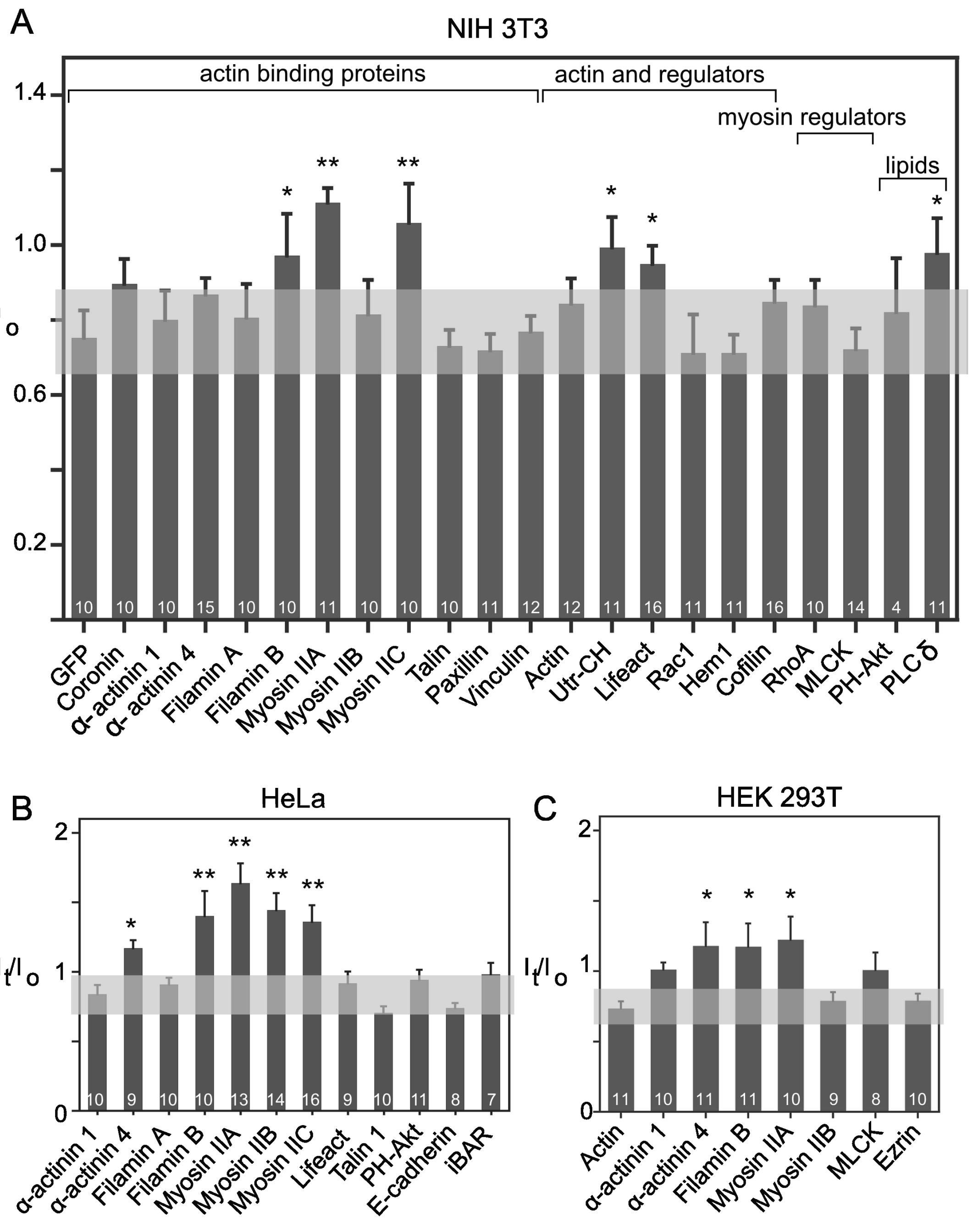

Figure 2.2. Actin-binding proteins respond most-strongly to externally-applied mechanical stress. Related to Figure 2.1. (**A**) In NIH 3T3 cells, (**B**) HeLa cells, and (**C**) HEK 293T cells, α-actinin 4, filamin B, and myosins IIA and IIC showed the most robust accumulation. The peak accumulation of myosin IIB varied between cell types (n values noted on bars, $*p<0.05$, $**p<0.005$).

exists, which is likely to be the network that experiences these two modes of deformation (22). Maximal protein accumulation in response to dilational deformation was quantified by normalizing the fluorescence intensity of the cortex in the tip region (I_t) to that of the unstressed cortex opposite the pipette (I_o) (**Fig. 2.1**). The grey bar represents the 95% confidence interval for cytosolic GFP quantified in the same manner, a control used in all cell types to denote the threshold over which a protein must accumulate to be significantly mechanosensitive. The response of the majority of proteins fell within this confidence interval, implying their insensitivity towards dilational deformation in all cell types. The greatest accumulative responses were observed in actin-binding proteins, including the myosin IIs. The extent of myosin accumulation did not correlate with the radius of the pipette, ruling out accumulation due to specific local membrane curvature **(Fig 2.3D)**. In addition, the curvature-sensing protein i-BAR showed no accumulation (**Fig 2.2B**), supporting the notion that the observed accumulations are due to mechanical stress sensing rather than curvature sensing. We selected the highly accumulative myosin II, α-actinin, and filamin for further characterization.

Non-muscle myosin II mechanosensation

Non-muscle myosin II is an established part of a mechanosensitive system both in *Dictyostelium* and *Drosophila*, where it accumulates at the site of applied forces and drives cellular contraction (18, 39, 46, 70). The magnitude of accumulation depends on the net force on each myosin II head and requires the presence of actin-crosslinkers to anchor actin filaments (18, 40, 41, 56). Mammalian cells express three paralogs of non-muscle myosin II: IIA (MYH9), IIB (MYH10), and IIC (MYH14). By examining differences in accumulation of these paralogs across multiple cell lines during MPA, we aimed to uncover how the mechanoresponsiveness of this important mechanoenzyme is

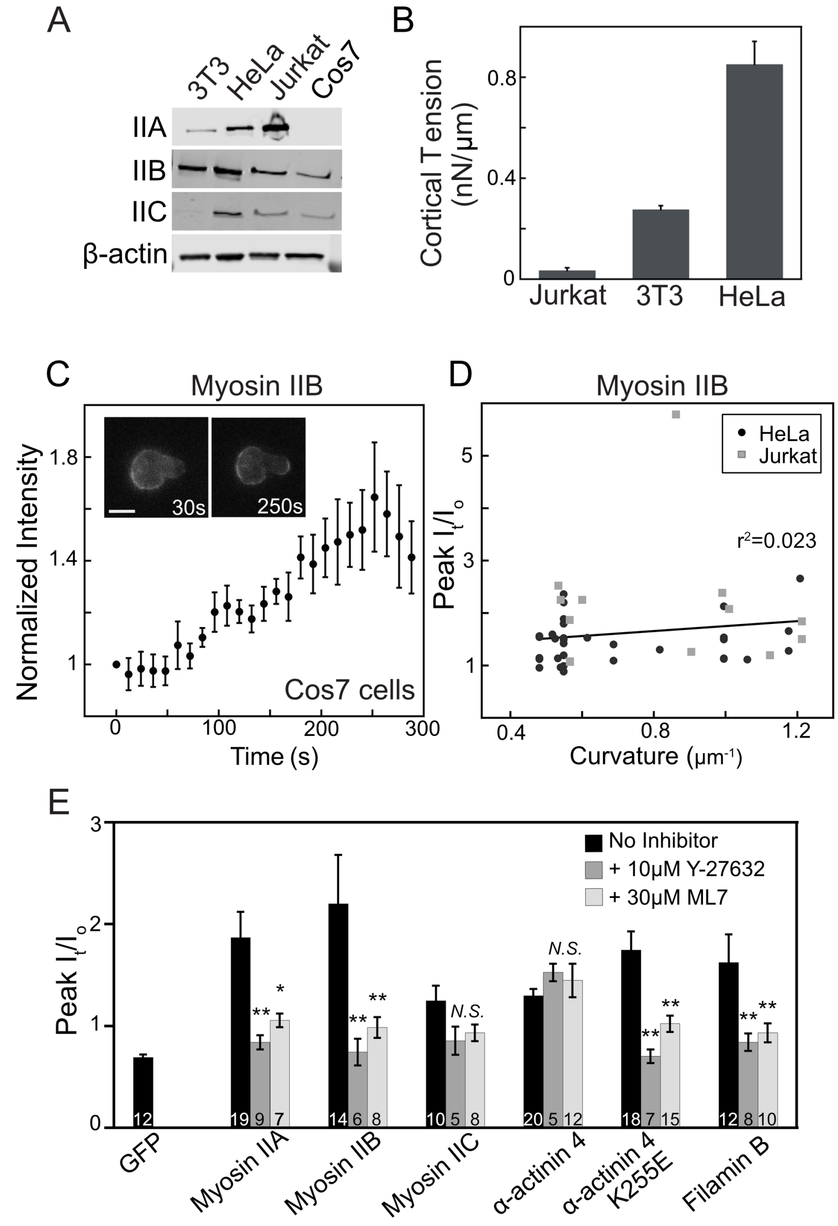

Figure 2.3. Myosin IIB mechanoresponse is not dependent on endogenous expression or myosin IIA mechanoresponse. Related to Figure 2.4. (**A**) Neither the endogenous expression of the three myosin II paralogs, (**B**) nor the resting cortical tension of Jurkat, NIH 3T3, and HeLa cells correlate with myosin IIB mechanoresponse (**Fig. 2.4B**). Because Cos-7 cells do not express myosin IIA (**A**), yet show robust myosin IIB accumulation to the tip (n=7) (**C**), myosin IIA expression is not required for the myosin IIB mechanoresponse. (**D**) The curvature of the cortex at the tip of cells was estimated as 2/r, where r is the radius of the pipette used for MPA. Curvature was then plotted against the peak accumulation of myosin IIB (I_t/I_o), demonstrating no correlation between curvature and myosin IIB accumulation at the tip. (**Fig. 2.4B**). (**E**) ML7 and Y-27632 treatments inhibit the peak tip accumulation (normalized to the intensity at the opposite side of the cell (I_t/I_o)) of myosin IIA, myosin IIB, α-actinin 4 K255E, and Filamin B, but not wild-type α-actinin 4, in Jurkat cells (*p<0.005, **p<0.0001 for inhibitor values compared to “No Inhibitor” values). While myosin IIC accumulated significantly in the absence of inhibitor compared with GFP (p<0.05, see Fig. 1), it did not accumulate significantly in the presence of ML7 (p=0.40) or Y-27632 (p=0.62).

regulated in mammalian cells. The paralogs have differing duty ratios (56), unique force-dependent affinities to F-actin (42), and distinct spatial distributions in migrating cells (56, 72, 73) suggesting non-overlapping roles for the myosin II paralogs. Several studies revealed that cells respond to their mechanical environment by modifying or regulating the expression of these distinct myosin IIs (65, 72, 74).

In response to dilational stress, we found myosin IIA and IIC exhibited a characteristic accumulation curve in all cell types, showing a short (30-70s) delay followed by a sigmoidal rise in protein intensity, plateauing by 150-200s (**Fig. 2.4A,C**). This biphasic behavior is characteristic of cooperative binding interactions, a behavior we previously modeled for *Dictyostelium* myosin II (47). The network stress-dependent stalling of myosin II heads in the strongly-bound state during the myosin power stroke gives rise to this cooperativity and promotes bipolar thick filament assembly (18, 40, 45, 46). Once the accumulated myosin II fully opposes the applied stress, the bound heads do not experience increasing stress, resulting in maximal accumulation (18, 47).

Interestingly, while the accumulation kinetics for myosin IIA and IIC were nearly identical between cell types, myosin IIB showed highly cell-type and cell-cycle-stage specific behavior. In Jurkats, myosin IIB was the most mechanoresponsive paralog, achieving greater than two-fold normalized intensity relative to the opposite cortex. In HeLa cells, myosin IIB accumulated moderately, while in NIH 3T3 cells, no appreciable accumulation was detected (**Fig. 2.4B**). This difference in accumulation did not correlate with endogenous expression levels (**Fig. 2.3A inset**) or the cortical tensions of the cell types (**Fig. 2.3B**). It is unlikely that the accumulation of any paralog can be attributed to co-assembly with another, given the consistent behavior of myosin IIA and IIC in cells endogenously expressing very different quantities of all three proteins. In fact, while the mechanoresponse of myosin IIB correlated with IIA expression for these first three cell types, Cos-7 cells, which lack myosin IIA (**Fig. 2.3A inset**), showed robust myosin IIB

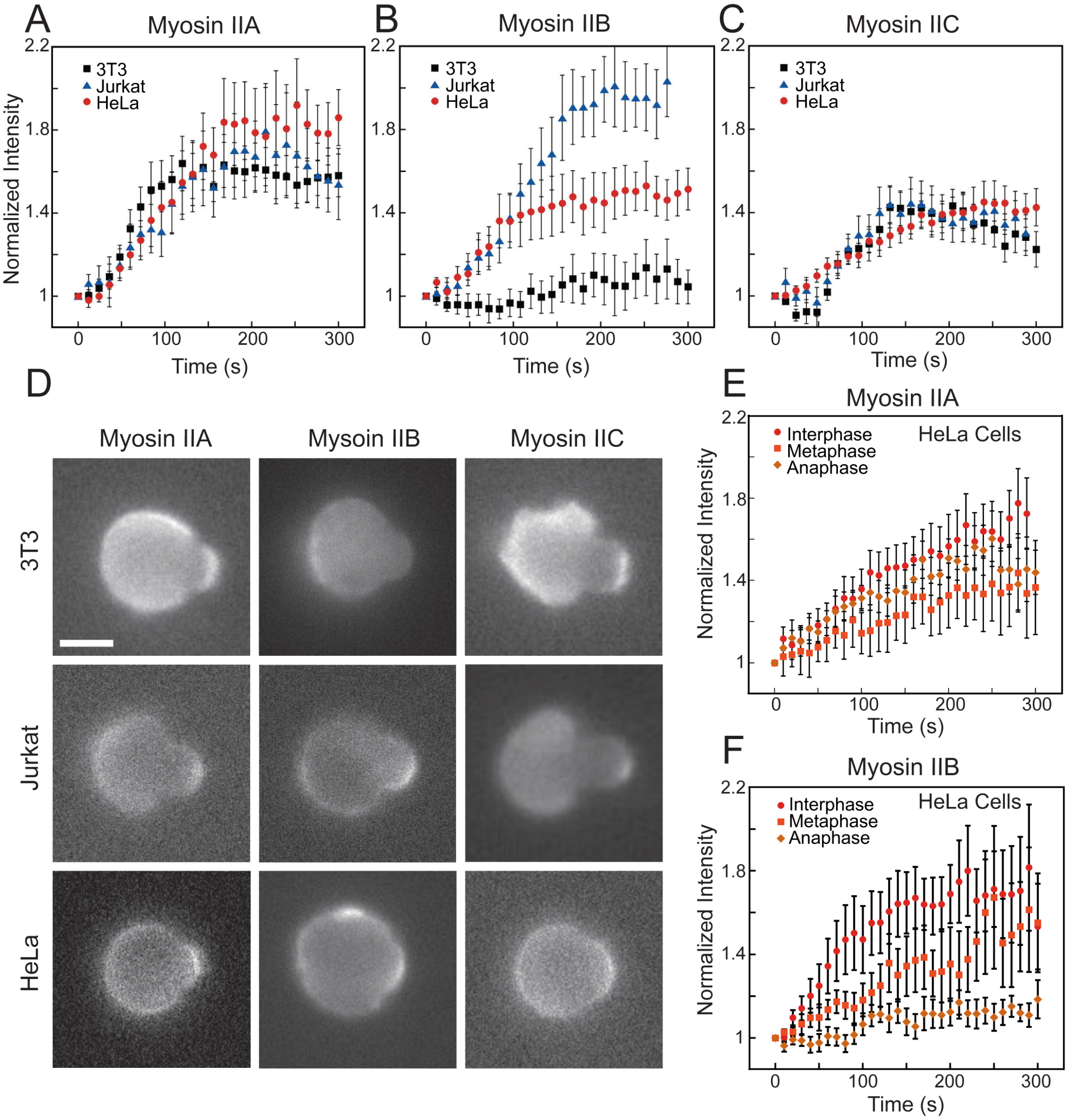

Fig. 2.4 Myosin IIA and IIC show mechanoaccumulation in all contexts examined, whereas myosin IIB shows mechanoaccumulation in distinct cell types and phases of the cell cycle. (**A**) Traces of myosin IIA and (**C**) myosin IIC accumulation over time (Normalized Intensity, I_t/I_o normalized to time zero) show initial sigmoidal kinetics indicative of cooperativity, followed by a late plateau, a curve which is similar in three distinct cell types: NIH 3T3 fibroblasts, Jurkat T-cells, and HeLas (n>10 cells/trace). (**B**) Myosin IIB shows distinct kinetics and levels of mechanoresponsive plateau in the three cell types (n>10 cells/trace). (**D**) Representative images of the maximum accumulation of GFP-labeled myosins shows a similar ratio of tip intensity to opposite cortex intensity for myosin IIA and IIC in all three cells, but a very different ratio for myosin IIB (scale bar = 10 μm). (**E**) Myosin IIA behaves similarly between the phases of the cell cycle induced by treatment with STLC (metaphase) STLC+Purvalanol (anaphase) or DMSO (interphase), while (**F**) myosin IIB becomes non-mechanoresponsive in anaphase (n>9 cells/trace).

accumulation (**Fig. 2.3C**), demonstrating that IIB's mechanoresponse is independent of

IIA. In addition, the accumulation of myosin IIB exceeded that of any other myosin II in Jurkat cells and did not accumulate in 3T3s despite the presence and accumulation of myosin IIA. Further, while myosin IIA showed no change in mechanoresponse over the cell cycle in HeLa cells (**Fig. 2.4E, Fig. 2.6A,B**), the myosin IIB mechanoresponse is cell cycle phase-specific; it accumulates in interphase and metaphase but not anaphase (**Fig. 2.4F, Fig. 2.6A,B**). This cell-cycle specificity implicates relatively transient regulatory mechanisms for the myosin IIB mechanoresponse that tune cellular shape-change during cytokinesis. One explanation is the phosphoregulation of IIB is distinct from that of IIA and IIC. Indeed, a short serine-rich stretch within the assembly domain of IIB confers its distinct localization pattern and behavior in cells in a phosphorylation-dependent manner (58), and this regulation could also affect myosin IIB mechanoaccumulation.

Paralog-specific mechanoresponsiveness of actin crosslinking proteins

Force sharing among actin crosslinkers is also important for cellular mechanoresponsiveness (18). From our search for mechanoresponsive elements, the actin crosslinkers α-actinin 4 and filamin B strongly responded. Interestingly, α-actinin 1 and filamin A did not accumulate significantly in any cell type. Thus, we examined what factors could lead to such paralog-specific differences. We previously characterized the force-dependent accumulation of the *Dictyostelium* α-actinin and filamin to dilated and sheared regions, respectively (18). In the absence of myosin II, we determined α-actinin strongly accumulated to dilated regions of the cell with significantly faster kinetics than myosin II. In contrast, filamin displayed rapid, cooperative, local enrichment in sheared regions at the pipette neck (18).

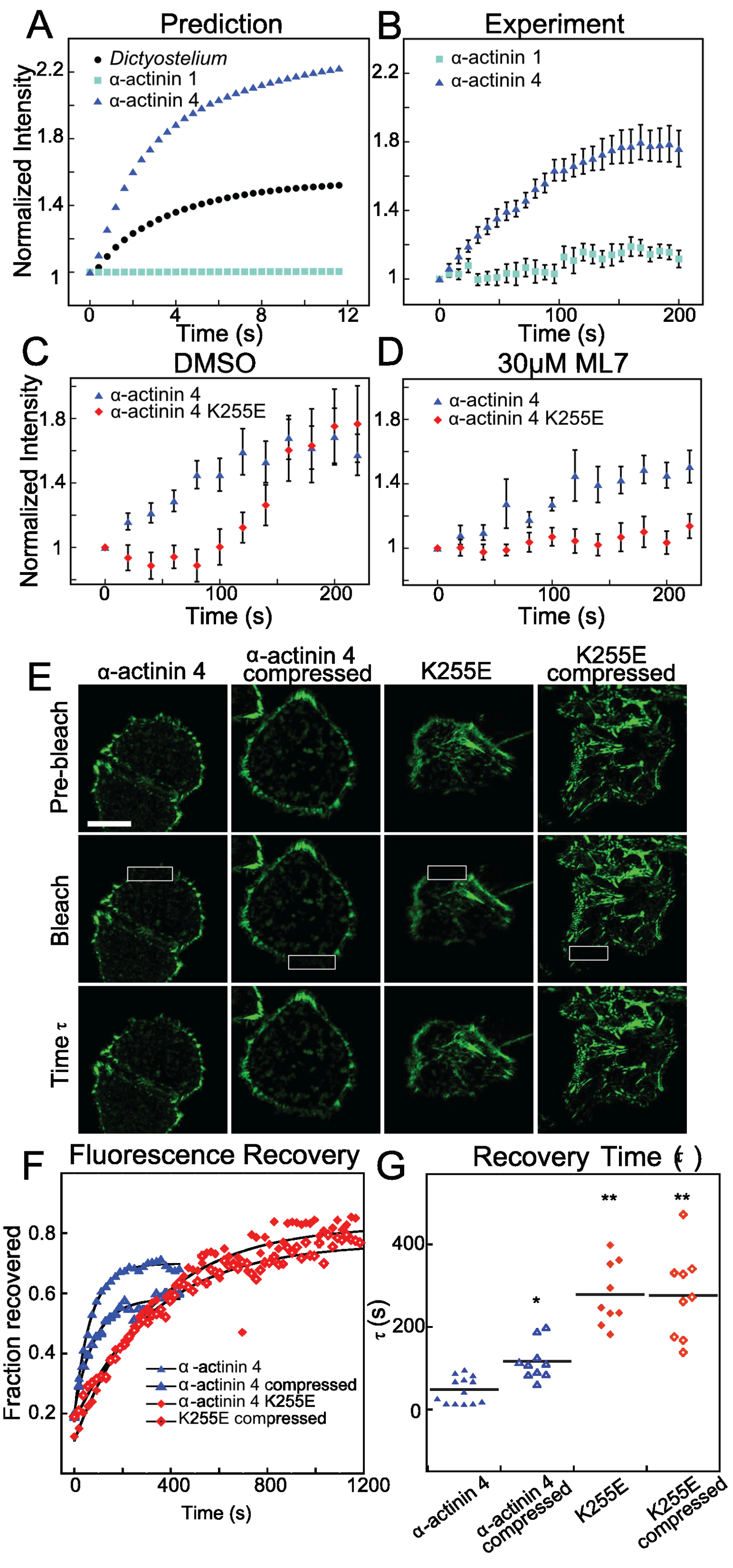

Fig 2.5. A force-dependent model based on actin binding affinity predicts the mechanoaccumulative behavior of α-actinins, and the high affinity α-actinin 4 mutant K255E is non-mechanoresponsive. (**A**) A reaction-diffusion catch-bond model of mechanoaccumulation derived from parameters outlined in *Dictyostelium* predicts high accumulation of mammalian α-actinin 4 and low accumulation of α-actinin 1 based on published actin-binding affinities. (**B**) This prediction captured both the protein behavior and shape of the curve in aspiration experiments in Jurkat cells (I_t/I_o normalized to time zero, n=12 cells/trace). (**C**) The α-actinin 4 K255E mutant has a five-fold higher binding affinity and shows delayed, myosin-dependent (**D**) accumulation as determined by using the pan-myosin **II** inhibitor ML-7 at 30 μM (n>16 cells/trace). Myosin accumulation was fully inhibited by ML-7 (**Fig. 2.3E**). (**E**) FRAP analysis of HeLa cells expressing GFP-α-actinin 4 and the K255E mutant in normal and compressed state. White boxes show bleached region at the time of bleaching, “Time τ” shows the level of fluorescence for each condition after one e-fold time of recovery as outlined in (**G**) (scale bar=10 μm). (**F,G**) Representative FRAP traces show a much faster recovery time for α-actinin 4 than K255E. The applied stress from agarose overlay drives slower recovery of α-actinin 4, but no change in K255E recovery (*p=0.001, **p<0.0001).

We modified a reaction-diffusion model first developed for *Dictyostelium* α-actinin (18) to predict mammalian α-actinin accumulative behavior (**Fig. 2.5A**), by using measured binding affinities for mammalian α-actinin 1 (K_d= 0.36 μM) or α-actinin 4 (K_d= 32 μM) without altering the other parameters. This model assumes the binding lifetime of α-actinin increases upon the application of force due to catch-bond behavior. Simulations of the model predicted that, owing to intrinsic differences in their initial binding affinities, α-actinin 4, but not α-actinin 1, would accumulate in response to deformation (**Fig. 2.5A**). During MPA, α-actinin 4 strongly accumulated in Jurkat cells with a curve shape strikingly similar to those in the simulations, while α-actinin 1 did not accumulate (**Fig. 2.5B**). However, the experimentally observed accumulation of α-actinin 4 was about 25 times slower than in the simulations. This difference is partly explained by a slower α-actinin rate of diffusion (3.7±0.2 $\mu m^2/s$ as measured by Fluorescence Correlation Spectroscopy (FCS) in **Figure 2.7D-F**, compared to 10 $\mu m^2/s$ used in the original model) and longer actin filaments in the mammalian cytoskeleton compared with *Dictyostelium* (75). To fully recapitulate the experiment, the on and off rates of actin-binding had to be slowed eight-fold, suggesting a level of mammalian α-actinin regulation not seen in *Dictyostelium* (**Fig. 2.7A**).

Here, through the use of modeling, we showed the initial binding affinity of an actin crosslinker dictates its general mechanoaccumulative behavior. In the model, the rapid accumulation of the lower-affinity α-actinin 4 is driven by a high rate of exchange with the actin network and a large pool of the unbound species. This dynamic crosslinker exchange can explain the rapid and dramatic changes in localization as the crosslinkers lock onto the network in response to mechanical stress. Further, actin-binding affinity must be low enough for there to be an available pool of cross-linkers for mechanoaccumulation to occur, but high enough for the protein to bind; hence a Goldilocks zone of affinity is suggested – not too high, not too low, just right.

To probe the molecular mechanism of α-actinin catch-bond behavior, we analyzed the α-actinin actin-binding domain (ABD), which is highly conserved among actin binding proteins (76). This domain consists of two calponin homology (CH) domains, each with an actin-binding site, that are normally tethered in a closed conformation by a salt bridge at the CH-CH interface. A mutation of lysine-255 to glutamate (K255E) in α-actinin 4 disrupts this salt bridge, driving the molecule into a permanently open configuration and revealing a third actin-binding site. *In vitro*, the K255E mutant has a five-fold higher actin binding affinity than the wild-type protein(77, 78). We hypothesized that network stress disrupts the salt bridge and converts the protein into the open, high affinity conformation, giving rise to catch-bond behavior of WT α-actinin 4 and leading to localized, stress-dependent accumulation. To test this, we analyzed the mechanoaccumulation kinetics of the K255E mutant, which we hypothesized lacks this mechanosensitive switch. Indeed, α-actinin 4 K255E did not accumulate in the first 100 s of aspiration. However, the mutant began to accumulate after 100 s (**Fig 2.5C**) with accumulation kinetics mirroring those of myosin II (**Fig. 2.4**). Therefore, we tested the role of myosin II by inhibiting the mechanoresponse of the three myosins with the myosin light chain kinase inhibitor ML7 (**Fig. 2.3E**). Upon the addition of 30 μM ML7, wild-type α-actinin 4 protein still accumulated considerably, while the K255E mutant did not (**Fig. 2.4D**). To rule out off-target effects of ML7, we independently verified the result using 10 μM Y-27632, an inhibitor of the Rho-associated kinase ROCK, which also regulates myosin light chain phosphorylation. The results were nearly identical for the two inhibitors **(Fig. 2.3E).** The model predicts that a simple five-fold change in actin-binding affinity would not prevent α-actinin 4 accumulation (**Fig. 2.7B**), suggesting the K255E mutation perturbs α-actinin's mechanism of mechanoresponse.

To assess the necessity of the salt bridge for catch-bonding, we analyzed the fluorescence recovery after photobleaching (FRAP) of both wild-type and mutant α-actinin 4 in HeLa cells in the absence or presence of compressive stress (**Fig. 2.5E**).

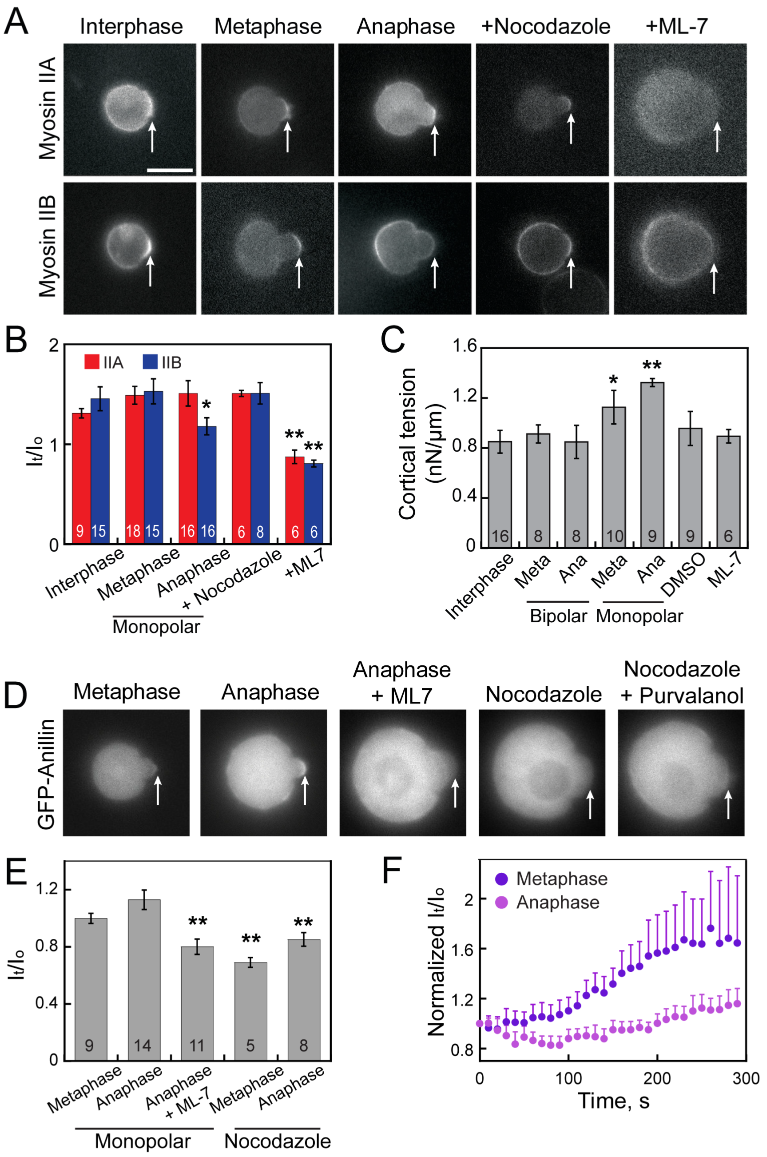

Figure 2.6. Mechanoresponsiveness of myosin II and anillin in HeLa cells. Related to Figure 2.4. (**A**) Representative micrographs of micropipette aspiration on HeLa cells transiently expressing GFP-myosin IIA or IIB. Nocodazole treatment induces metaphase arrest so these cells are also in metaphase. (Scale bar = 10 μm). (**B**) Average ratio of GFP-myosin II mean intensity at the tip to that at the opposite cortex for aspirated HeLa cells. (**C**) Cortical tension measurements using micropipette aspiration for interphase and mitotic HeLa cells. DMSO and ML7 measurements were performed on interphase cells. (**D**) Representative micrographs of micropipette aspiration on HeLa cells stably expressing GFP-anillin. (**E**) Average ratio of GFP-anillin mean intensity at the tip to that at the opposite cortex. (**F**) Kinetic traces for anillin's mechanosensitive accumulation (normalized to t = 0 s) in monopolar mitotic cells. n value is listed on bars; n for each kinetic trace is the same as listed on corresponding bar in (**E**) (*$p < 0.05$, **$p < 0.005$).

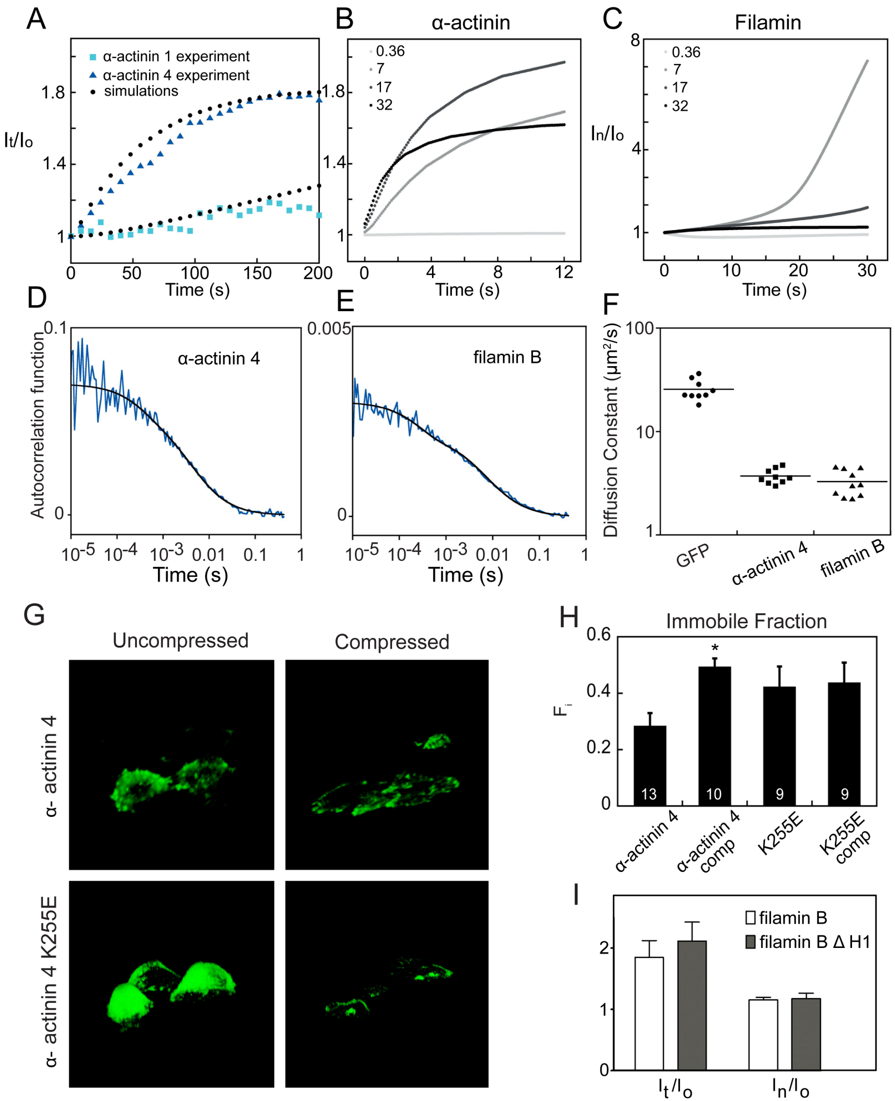

Figure 2.7. Modeling and measuring the mechanisms of filamin and α-actinin mechanoresponse. Related to Figures 2.5 and 2.8. (**A**) The simulations for α-actinin 1 and α-actinin 4 match the experimentally observed accumulation curve when the on and off rates are slowed by a factor of 8, preserving each protein's K_d. (see **Fig. 2.5B**). (**B**) For both α-actinin and (**C**) filamin, a catch-bond model predicts poor accumulation at very high binding affinities (K_d = 0.36μM), presumably due to a lack of free monomer in the cytoplasm. (**B**) The K_d of α-actinin 4 (32μM) predicts robust accumulation in the non-cooperative α-actinin model, (**C**) but poor accumulation in the cooperative filamin model. The K_d of filamin B and α-actinin 4 K255E (7μM) predicts accumulation in both models. (**C**) The K_d of filamin A (17μM) predicts no accumulation in the filamin model. Thus, both very high and very low K_d values can inhibit filamin's mechanoaccumulation; the K_d at which the most robust accumulation occurs depends on whether the model is non-cooperative (α-actinin, **Fig. 2.5B**) or cooperative (filamin, **Fig. 2.8B**) (**D**) Representative correlation curve measured by FCS for α-actinin 4 in Jurkat cells and (**E**) filamin B in HeLa cells. (**F**) Measured diffusion constants for GFP (26±2.0), α-actinin 4 (3.7±0.20), and filamin B (3.3±0.30). (**G**) Rotated view of a 3D projection of Hela cells, which are flattened to an approximate height of 2 μm when compressed with a sheet of 1% agarose 0.2 mm thick for **Fig. 2.5E-G.** (**H**) Compressed α-actinin 4 showed a higher immobile fraction (*p=0.007), while there was no significant difference between the immobile fraction of the K255E mutant with and without compression (n values noted on bars). (**I**) A mutant lacking the hinge region of filamin B did not show a difference in accumulation to the tip (I_t/I_o) or the neck (I_n/I_o) of the aspirated Jurkat cell (n=9).

Cells were compressed with a thin sheet of agarose, reducing their height by a roughly a factor of 2. We have demonstrated previously that this technique drives the accumulation of mechanosensitive proteins, including myosin II and cortexillin, to the cell's lateral edges where dilation is highest (18) as the cell actively resists the applied load (22). Although the exact force felt by the cytoskeleton is difficult to quantify in this technique, the recovery time (τ) of proteins that lock onto the cytoskeleton under physiologically-relevant applied loads increases (22). The K255E mutant localized to stress fibers more readily than the wild-type even without applied stress, but all FRAP measurements were taken from the cell cortex (**Fig. 2.5E**). Similar to a previous report

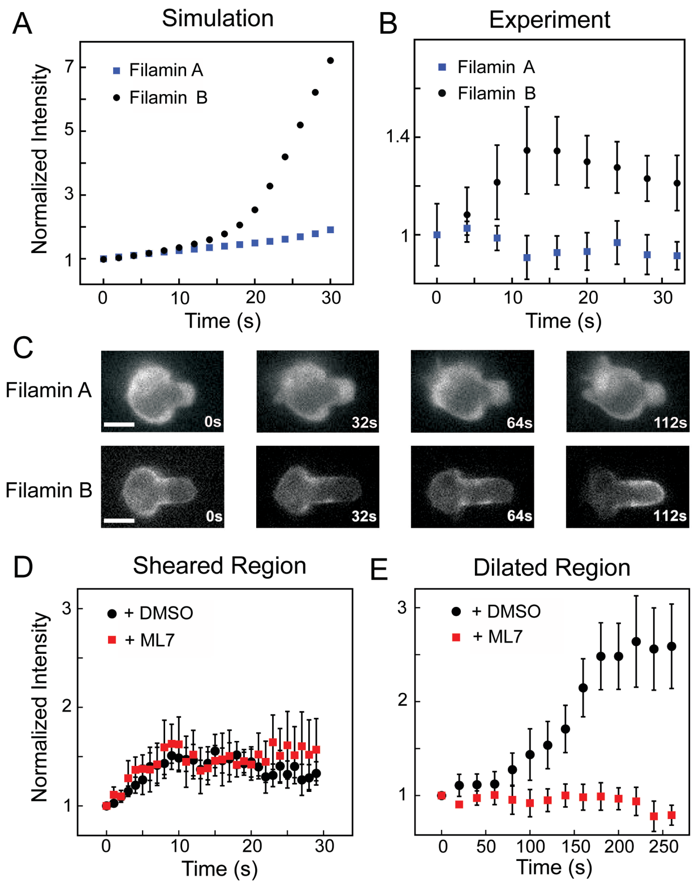

Figure 2.8. A force-dependent model based on actin binding affinity predicts the mechanoaccumulative behavior of filamins to a region of shear deformation, followed by myosin driven cell tip accumulation. (**A**) A cooperative reaction-diffusion catch-bond model of mechanoaccumulation predicts low accumulation of filamin A and high accumulation of filamin B to the neck region of the cell, where shear deformation is highest. (**B**) In Jurkat cells, filamin A does not accumulate appreciably while filamin B accumulates to the cell neck, though initial accumulation was followed by a decay phase (I_n/I_o normalized to time zero, n=10). (**C**) This decay phase resulted from flow of filamin B, but not filamin A, from the cell neck to the cell tip (scale bars = 10 μm). (**D**) Accumulation to the cell neck was not myosin dependent (n=10). (**E**) However, flow to the cell tip was myosin II dependent. Cells in **D** and **E** were treated with DMSO or the pan-myosin II inhibitor ML-7 at 30 μM (n=12).

(78), the higher affinity K255E mutant showed much slower recovery than wild-type (**Fig 2.5F,G**). Interestingly, while wild-type α-actinin 4 showed slower recovery under agarose overlay, the K255E mutant showed no significant change in recovery time (τ) or immobile fraction (**Fig. 2.5F,G, Fig. 2.7H**). Thus, the catch-bond behavior of α-actinin 4 is most likely dependent on the conversion of the highly conserved ABD from a closed to an open conformation, a change regulated by the salt bridge. In addition, a late, myosin-dependent cortical flow phase is responsible for moving the higher affinity K255E mutant to the tip region, a phenomenon we also observed with filamin (see below).

Paralog-specific mechanoresponsiveness of filamin

In mammalian cells, non-muscle filamins A and B form Y-shaped dimers which orthogonally crosslink actin filaments (79). We previously found that *Dictyostelium* filamin, which forms a similar V-shaped dimer, is sensitive to shear deformation. This sensitivity manifests as an accumulation to the neck of the cell being deformed (18). The reaction-diffusion model for filamin included cooperativity and predicted robust accumulation of the higher affinity filamin B (K_d= 7 μM), and reduced accumulation of lower-affinity filamin A (K_d= 17 μM) (**Fig. 2.8A**). This is in contrast with the stronger accumulation for lower affinity α-actinin 4. While both α-actinin (non-cooperative) and filamin (cooperative) models unveil a Goldilocks zone for which the K_d is optimal for accumulation, the K_d that allows the most robust accumulation for each protein depends on whether cooperativity is present (**Fig. 2.7B,C**).

We were initially surprised to find that mammalian filamin B accumulated at the tip of the cell in our studies in Jurkats, instead of the neck region. Upon closer analysis, we noted that within 15 s of the pressure application, filamin B accumulated to the aspirated cell neck (**Fig. 2.8B**). The kinetics of this accumulation showed acceleration (**Fig. 2.8B**), suggesting cooperativity exists between neighboring actin-bound filamin B molecules.

Longer-term tracking revealed that filamin B flows from the neck to the tip of the cell along the cortex (**Fig. 2.8C,E**), a process not observed in *Dictyostelium*. Filamin A failed to respond to applied pressure (**Fig. 2.8B,C**). Since the time scale for the tip accumulation of filamin B is ~80 s (**Fig. 2.8E**), along myosin II's time scale, we hypothesized that filamin B accumulation in the tip was driven by myosin II accumulation. Upon the addition of 30 μM ML7 or 10 μM Y-27632 **(Fig. 2.3E)**, filamin B showed normal neck accumulation (**Fig. 2.8D**) but did not accumulate to the tip (**Fig. 2.8E**). It has been shown that a filamin A mutant lacking the hinge 1 region fails to cause strain stiffening induced by its wild-type counterpart (80). However, in our experiments, the filamin B hinge mutant showed wild-type mechanoaccumulation to either the neck or the tip of the cell (**Fig. 2.7I**), indicating shear-force sensation does not depend on this hinge. Thus, filamin B shows both rapid, intrinsic, shear deformation-sensitive accumulation at the cell neck, as well as myosin II-dependent cortical flow to the tip of the cell upon applied force. This myosin-dependent cortical flow resembles that seen in the α-actinin 4 K255E mutant; these two proteins have similar affinities for actin (K_d≈7 μM), which may allude to the requirement of a specific actin-binding affinity in order to be acted upon by the myosin-dependent flow. In HeLa cells, the important cytokinesis-regulator anillin also responds to the tip of the pipette, but does so exclusively during anaphase in a myosin-dependent manner (**Fig. 2.6D-F**). This implies a biological role for myosin-dependent accumulation in mammalian cytokinesis. These myosin-driven cortical network flows are similar to those essential for proper asymmetric cell division during *C. elegans* development (81).

Conclusions

In this study, we uncovered mammalian mechanosensors that accumulate under mechanical stress. We identified a Goldilocks zone of actin-binding affinities, determined by their cooperative or non-cooperative binding properties, which dictates the maximal accumulation of these elements. We discovered two distinct modes of force-dependent accumulation: a rapid, diffusion-based mode dependent on molecular catch-bonding behavior, and a slower, myosin II-dependent cortical flow which drives actin-binding proteins to the cell tip. We also discovered the cell-type- and cell-cycle-specific mechanosensitivity of myosin IIB, which is intriguing in light of studies implicating myosin IIB as a driver of breast-cancer metastasis (82). In Chapter 3, we will uncover how heavy-chain phoshoregulation of myosin IIB contributes to this mechanoresponsive pattern.

CHAPTER 3. PKCζ PROVIDES SETPOINT CONTROL FOR MYOSIN IIB MECHANOSENSITIVE DYNAMICS

As covered in Chapter 2, non-muscle myosin II senses and accumulates in response to mechanical inputs during cytokinesis and cell migration, which allows for the proper spatial localization and function of the protein (18, 41, 44, 46, 49, 65, 83). Interestingly, signaling pathways—such as Cdc42/mPAR6/PKCζ—can directly impact the dynamics of the non-muscle myosin II pool (58, 84). Understanding how this chemical regulation affects the ability of non-muscle myosin II to bind specifically to actin filaments experiencing mechanical load is key to determining the molecular mechanism by which non-muscle myosin II is tuned to localize correctly in cells during shape-change processes.

In the social amoeba *Dictyostelium discoideum*, the regulation of myosin II (myoII) turnover and localization during cytokinesis and chemotaxis is controlled by the phosphorylation of three threonine residues in the myoII heavy chain helical tail region by the myosin heavy chain kinases (MHCKA, MHCKB, MHCKC, MHCKD; (85). A mutant myosin II protein containing aspartic acids at all three threonine residues to mimic phosphorylation (3xAsp) form very limited bipolar filaments *in vitro*, shows very little enrichment in the actin cortex in cells, and does not accumulate at the furrow during cytokinesis (60, 86, 87). In contrast, a myosin II mutant protein containing nonphosphorylatable alanine residues at the three critical threonines (3xAla) shows higher assembly into bipolar filaments than wild-type and over-accumulates in the cell cortex and cleavage furrow (60, 86, 87). In this study, to emulate the mechanical stresses that cells produce internally or experience externally without probing substrate adhesion-based signaling, we again use micropipette aspiration (MPA). Using this method, wild-type GFP-MyoII accumulates in response to imposed stress, but the under-assembled GFP-3xAsp and the over-assembled GFP-3xAla mutants do not (40). This result indicates a critical relationship between myosin II assembly/disassembly dynamics and mechanoresponsiveness, and that the setpoint of myosin II assembly and mechanoresponse is controlled by myosin heavy chain kinase activity.

In mammalian cells, the three non-muscle myosin II paralogs - NMIIA, NMIIB, and NMIIC - are regulated by RLC and heavy chain phosphorylation (56, 88). Spatially-broad force-dependent activation of NMII through phosphorylation of the RLC has been demonstrated (56, 89). Certainly, RLC phosphorylation is required for myosin II mechanoresponsiveness in *Dictyostelium* and mammalian cells (39, 40, 49). Inhibition of RLC phosphorylation by inhibiting calcium-activated MLCK or RhoA-activated ROCK, inactivates and prevents force-dependent accumulation of all three mammalian NMIIs (49). However, RhoA, ROCK, and MLCK do not show mechanosensitive accumulation and calcium signaling is not required for myosin's mechanoaccumulation (18, 39, 49). Thus, even though RLC phosphorylation is essential for activating myosin, it does not specifically direct myosin binding to actin filaments experiencing tension. Instead, mechanical stress directly promotes the cooperative binding of myosin II to actin in *Dictyostelium*, *Drosophila* and mammalian cells (39, 42-45, 90).

Furthermore, as discovered in Chapter 2, the mammalian NMIIs show paralog-specific regulation of mechanoresponsiveness. The peak accumulation of NMIIA and NMIIC during MPA is very similar across multiple mammalian cell types and across the cell cycle. However, the peak accumulation of NMIIB is differentially regulated across cell types and phases of the cell cycle (49). Thus, this unique behavior cannot be explained by RLC activation as the three NMII isoforms share the canonical calcium- and RhoA-dependent mechanisms of RLC phosphorylation (56). This myosin paralog-specific mechanoresponsiveness, in combination with the importance of heavy chain regulation-dependent mechanoresponse in *Dictyostelium* (40), led us to investigate the influence of NMIIB heavy chain phosphoregulation on mechanoresponsiveness.

The NMII heavy chain tail is phosphorylated by PKC, casein kinase II, and TRPM7 enzymes (56). Phosphorylation of the NMIIA tail by PKCβ results in paralog-specific binding by S100A4 (or mestastasin 1, Mts1) and increased NMIIA filament turnover (56). For NMIIB, paralog-specific phosphorylation by the atypical PKCζ leads to slower filament assembly and altered NMIIB organization in cells (84). Phosphomimetic NMIIB mutants mimicking PKCζ phosphorylation (1935D) show faster turnover in cells by Fluorescence Recovery After Photobleaching (FRAP) and altered localization during migration (58). NMIIB localization is PKCζ-dependent, as an overactive version of the kinase (myristoylated-PKCζ) alters the morphology of migrating cells expressing wild-type NMIIB but has no effect on cells expressing the non-phosphorylatable mutant, NMIIB 1935A (58). Here, we show that by controlling the assembly of NMIIB in bipolar filaments that associate with the actin cytoskeleton, PKCζ-dependent heavy chain phosphorylation provides setpoint control for NMIIB mechanoresponsiveness.

Myosin II heavy chain phosphorylation controls mechanoresponse in *Dictyostelium* in a biphasic manner

In beginning to decipher how NMIIB setpoint control might work, we noticed a trend in the *Dictyostelium* system that provides powerful insight. In Ren *et al.,* 2009, myosin II heavy chain null *(myoII*) *Dictyostelium* cells expressing N-terminal GFP-labeled wild-type myosin II were aspirated by MPA, and the GFP-myoII responded by accumulating in the pipette in response to the applied stress (**Fig. 3.1A**). In contrast, GFP-3xAsp or GFP-3xAla proteins did not accumulate in response to applied stress (**Fig. 3.1A**). Mechanoresponsiveness for these mutants in the MPA assay was quantified using a ratio of the peak background-corrected fluorescence intensity in the pipette to the

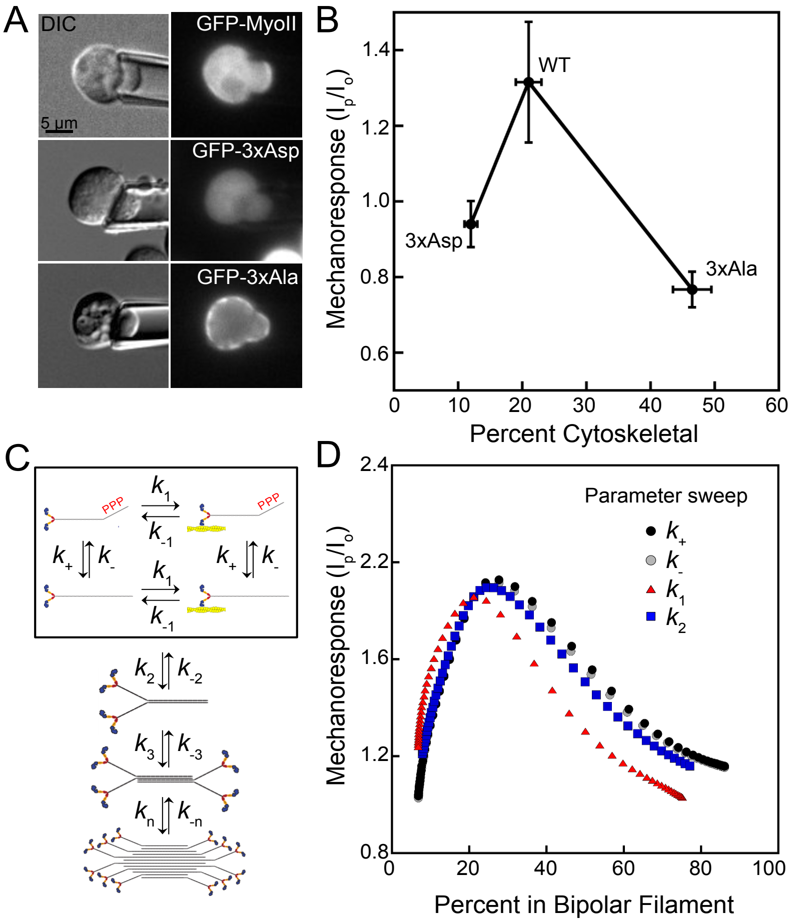

Figure 3.1. Myosin II cytoskeletal association and mechanoresponsiveness have a biphasic relationship in *Dictyostelium*. (A) GFP-MyoII accumulates to the region of the cell dilated by the pipette upon applied force. MyoII mutants mimicking heavy chain phosphorylation (GFP-3xAsp) or non-phosphorylatable mutants (GFP-3xAla) do not respond to the applied force. **(B)** Mechanoresponsiveness has a biphasic dependency on the percentage of myosin that is cytoskeleton-associated. Peak myosin II mechanoresponse is calculated as the highest ratio of background-subtracted intensity in the pipette (I_p) to the background-subtracted intensity at the cortex at the opposite side of the cell (I_o) in 5 minutes, and are reproduced from Ren *et al,* 2009 with permission. Percent cytoskeletal is measured by cytoskeletal fraction and reproduced from Rai and Egelhoff, 2011 with permission. **(C)** Scheme to model the assembly of myosin II bipolar filaments, including exchange between assembly-incompetent, assembly competent, actin-bound, and actin-unbound monomers (boxed). Monomers then assemble into dimers, tetramers, and bipolar filaments. **(D)** A computational model for myosin II mechanosensitive assembly predicts that when increased or decreased by an order of magnitude, rates affecting myosin II transition from assembly-incompetent to assembly-competent (k_+, k_-), from actin-unbound to actin-bound (k_1), or from monomer to dimer (k_2) will reproduce a biphasic relationship between the percent of myosin II assembled and the mechanoresponse at 5 minutes.

intensity of the cortex at the opposite side of the cell (I_p/I_o) (40). Cytoskeletal association of these mutants had also been measured previously via cytoskeletal fractionation (91). When we compiled these observations by plotting the mechanoresponsiveness as a function of percentage of myosin II in the cytoskeletal fraction, we observed a biphasic relationship (**Fig. 3.1B**). Very poor mechanoresponsiveness was observed when myosin II cytoskeletal association was low (12%, GFP-3xAsp) or high (47%, GFP-3xAla). However, wild-type GFP-myoII had high mechanoresponsiveness but had intermediate cytoskeletal association (21%, wild-type GFP-myoII).

To validate this biphasic relationship between degree of cytoskeletal association and the myosin II's mechanoresponsiveness, we leveraged a computational model we developed previously to describe mechanosensitive accumulation of myosin II in *Dictyostelium* (18, 41, 47)*.* The model describes bipolar filament formation from the monomers to filaments consisting of up to 36 dimers in the mature bipolar filaments. Monomers are assumed to be in one of four states, depending on whether they are bound to actin or not, and/or assembly competent or incompetent (**Fig. 3.1C**). We also consider that the detachment of bound myosin from actin is force-sensitive. Spatially, we compartmentalize the cell into three regions: the cytosol, and two separate cortex regions, depending on whether the cortical regions are under mechanical stress or not. Simulations were used to compute the fraction of myosin in filaments and the ratio of myosin between the cortex at the site of applied stress over the site without stress. At the nominal parameter values, the fraction of myosin in bipolar filaments was 21% and the ratio between myosin cortex concentrations was 1.9 (the point at which all curves intersect in **Fig. 3.1D**). These simulations were then repeated while varying several of the parameters describing rates of monomer and dimer interconversion one order of magnitude above and below nominal values (**Fig. 3.1D**). In all cases, mechanosensitive accumulation vs. filament formation displayed the same biphasic pattern seen experimentally, with the peak mechanosensitive accumulation occurring between 20-25% assembly.

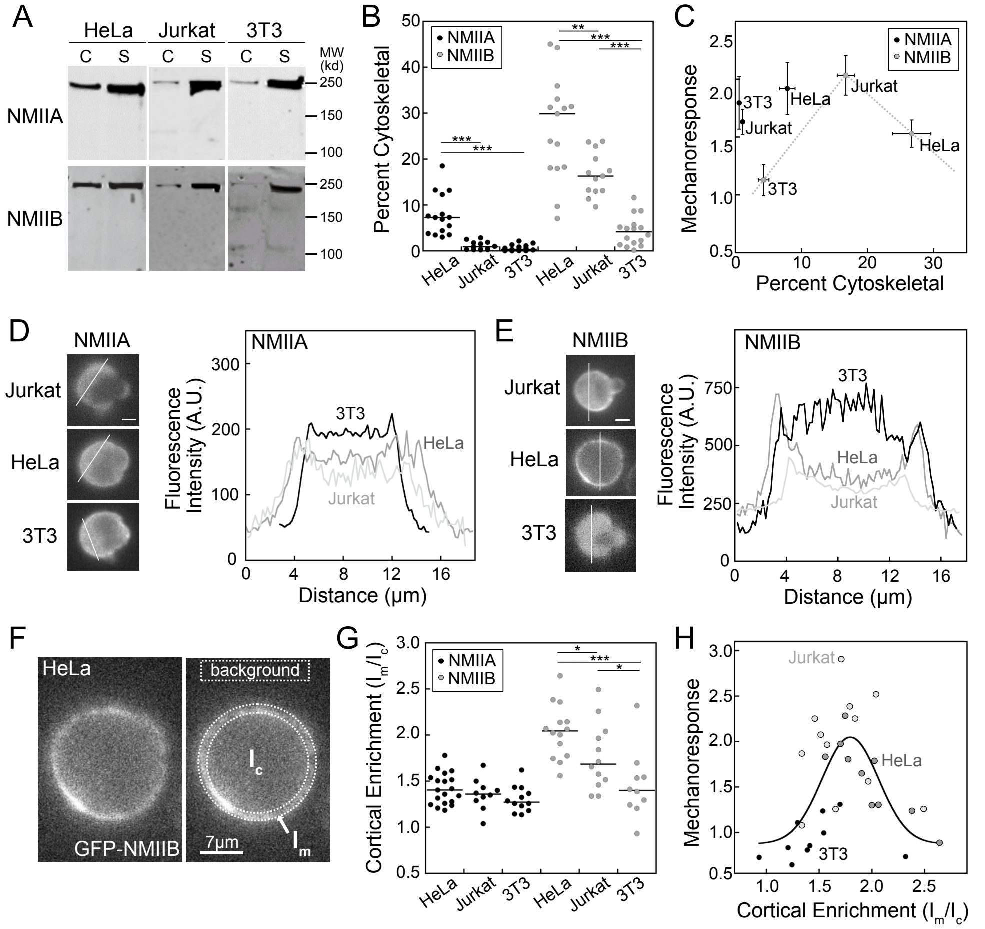

Figure 3.2. Myosin IIB cytoskeletal enrichment predicts mechanoresponsiveness in mammalian cells in a biphasic manner. (A) Representative cytoskeletal assembly assay westerns quantified in **(B)**, which shows median cytoskeletal association less than 10% for NMIIA, and highly divergent median cytoskeletal association for NMIIB in HeLa, Jurkat, and NIH 3T3 cells. **(C)** Plotting peak mechanoresponse (I_p/I_o) against percent cytoskeletal shows that NMIIB mechanoresponse is optimal in Jurkat cells, which have moderate cytoskeletal association among the three cell types. NMIIA shows no such relationship. **(D)** Representative intensity line scans of GFP-NMIIA or **(E)** GFP-NMIIB at the initial frame of an MPA experiment demonstrate low initial cortical enrichment in three cell types for GFP-NMIIA, but divergent cortical enrichment for the three cell types for GFP-NMIIB. **(F)** Representation of the quantification of cortical enrichment by comparing background-subtracted mean intensity in the membrane region (I_m) to that of the cytosolic region (I_c). **(G)** Quantification of cortical enrichment (I_m/I_c) in three cell types show no significant differences for GFP-NMIIA, but differences in GFP-NMIIB highly similar to the differences in panel **(B)**. **(H)** Plotting each cell's peak mechanoresponse (I_p/I_o) as a function of its initial cortical enrichment value (I_m/I_c) shows a biphasic distribution similar to a Gaussian function. *$p<0.05$, **$p<0.005$, ***$p<0.0005$.

NMIIB cytoskeletal enrichment predicts mechanoresponsiveness in mammalian cells in a biphasic manner

To investigate the cell-type specific mechanoresponsiveness of NMIIB demonstrated previously (49), and in light of the impact of myosin II cytoskeletal association on mechanoresponsiveness observed in *Dictyostelium* (**Fig. 3.1**; (40, 91), we quantified the cytoskeletal association of myosin II in HeLa, Jurkat, and NIH 3T3 cells. HeLa, Jurkat, and NIH 3T3 cells were gently lysed and subjected to cytoskeletal fractionation, and the cytoskeletal and supernatant fractions were probed for NMIIA or NMIIB (**Fig. 3.2A**). All three cell types showed less than 10% association of NMIIA with the cytoskeleton, and stronger cortical association of NMIIB than NMIIA (**Fig. 3.2B**). HeLa cells showed the highest NMIIB cytoskeletal association (27±2.8%), followed by Jurkat cells (17±1.3%) and NIH 3T3 cells (4.3±0.81%) (**Fig. 3.2B**). Peak NMIIB mechanoresponse in five minutes demonstrated biphasic behavior as a function of cytoskeletal association, reminiscent of the relationship seen in *Dictyostelium* (**Fig. 3.1**). NMIIA, on the other hand, showed no clear correlation (**Fig. 3.2C**).

To more closely probe the relationship between myosin cortical association and mechanoresponsiveness, we measured these two parameters in individual cells. Fluorescence intensity line scans across individual cells were performed at the time when cells are initially contacted with the pipette (t=0), avoiding the nucleus. NMIIA shows low cortical enrichment with very little variation between the three cell types (**Fig. 3.2D**). NMIIB shows very little cortical enrichment in NIH 3T3 cells, moderate enrichment in Jurkat cells, and heavy enrichment in HeLa cells (**Fig. 3.2E**). The level of enrichment was quantified for each cell by taking a ratio of background-corrected mean fluorescence intensity at the cell membrane to the intensity inside the cytoplasm (I_m/I_c) (**Fig. 3.2F, G**). While no significant difference was seen between the three cell types for NMIIA, NMIIB showed significant differences between each of the cell types (**Fig. 3.2G**). This trend closely resembles the cytoskeletal association measured at a population level in **Figure 3.2B**. Plotting each cell as a function of both peak mechanoresponse and cortical enrichment (I_m/I_c) shows that moderately enriched cells, with I_m/I_c values between 1.5 and 2.0, show the highest mechanoresponsiveness (**Fig. 3.2H**). Each cell type clusters distinctly, with NIH 3T3 cells on the far left of the Gaussian fit, Jurkat cells in the center and high on the curve, and HeLa cells falling on the right (**Fig. 3.2H**). Comparison of overall fluorescence intensity with mechanoresponsiveness in cells shows very poor correlation, indicating that the level of NMIIB expression has a minor effect on mechanoresponsiveness compared with assembly (**Fig. 3.3A**).

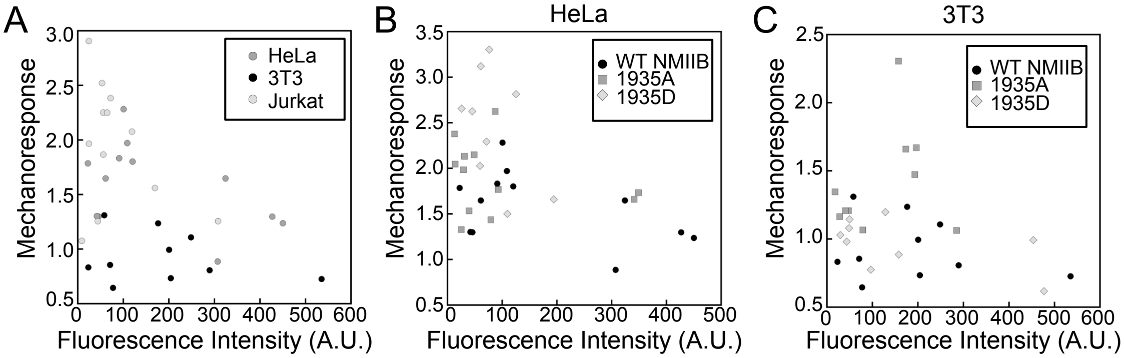

Figure 3.3. Magnitude of mechanoresponse is independent of intensity of GFP-NMIIB in cells. (A) In HeLa, NIH 3T3, and Jurkat cells, GFP-NMIIB fluorescence intensity is similar, and shows poor correlation with mechanoresponse. **(B)** In HeLa cells, GFP-NMIIB, GFP-NMIIB 1935A, and GFP-NMIIB 1935D fluorescence intensity is similar, and shows poor correlation with mechanoresponse. **(D)** In NIH 3T3 cells, GFP-NMIIB, GFP-NMIIB 1935A, and GFP-NMIIB 1935D fluorescence intensity is similar, and shows poor correlation with mechanoresponse.

NMIIB heavy chain phosphomimetic and non-phosphorylatable mutants change cortical enrichment and mechanoresponsiveness

To test whether altering the cortical enrichment of NMIIB is sufficient to change NMIIB mechanoresponsiveness in a single cell-type, we expressed GFP-NMIIB constructs with phosphomimetic and non-phosphorylatable mutations in the tail domain. In HeLa cells, the 1935D mutant showed reduced initial enrichment in the cortex compared to the 1935A mutant and much higher mechanoresponsiveness than the 1935A mutant over five minutes (**Fig. 3.4**). Quantification of the cortical enrichment (I_m/I_c) of the 1935D mutant showed a lower value than wild-type, while the 1935A mutant showed no change (**Fig. 3.4B**). Quantification of mechanoresponse kinetics was performed by normalizing

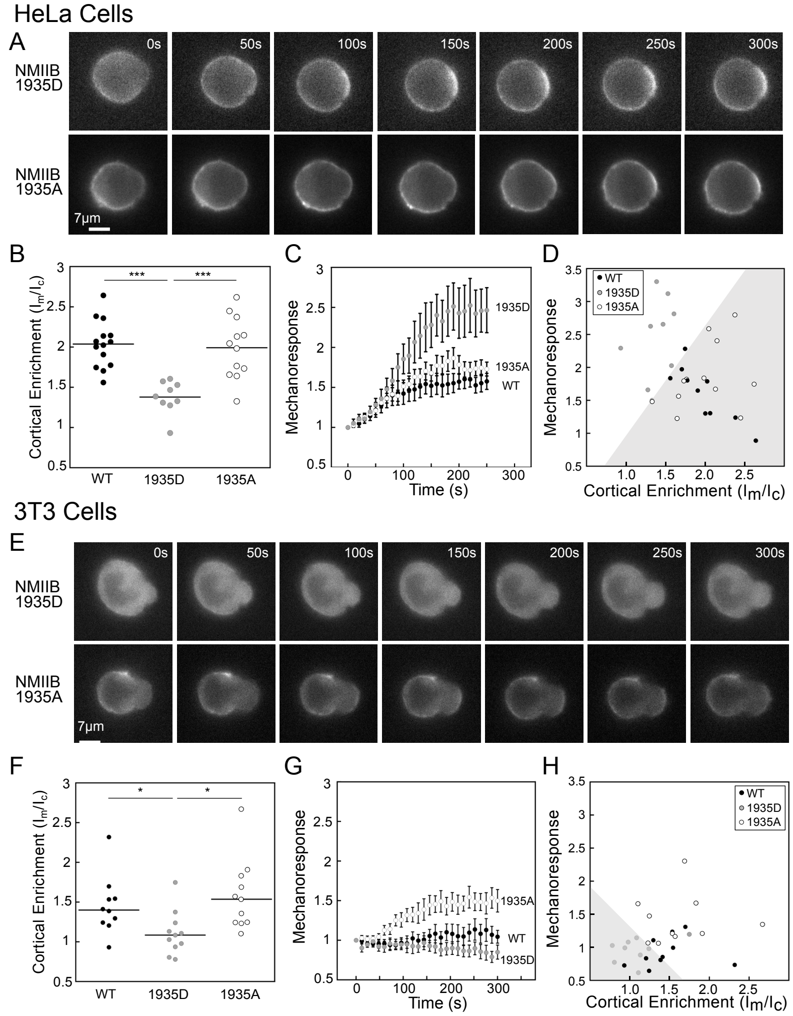

Figure 3.4. Myosin IIB heavy chain phosphomimetic and non-phosphorylatable mutants change cortical enrichment and mechanoresponsiveness. (A) Representative time series for MPA of HeLa cells expressing GFP-tagged phosphomimetic (NMIIB 1935D) or non-phosphorylatable (NMIIB 1935A) mutants of NMIIB. **(B)** Quantification of initial cortical enrichment (I_m/I_c) of NMIIB shows a highly significant reduction in cortical enrichment for the 1935D mutant, but not for the 1935A mutant, compared to wild-type GFP-NMIIB. **(C)** Accumulation during MPA over 250 seconds shows much more robust response for the 1935D mutant compared to the 1935A mutant or wild-type NMIIB. **(D)** Plotting peak mechanoresponse (I_p/I_o) and initial cortical enrichment (I_m/I_c) for each cell shows that all cells expressing the 1935A mutant are found in the lower right region of the graph (grey shaded area), while all cells expressing the 1935D mutant are found in the upper left region of the graph (unshaded region). **(E)** Representative time series for MPA of NIH 3T3 cells expressing GFP-tagged phosphomimetic (NMIIB 1935D) or non-phosphorylatable (NMIIB 1935A) mutants of NMIIB. **(F)** Quantification of initial cortical enrichment (I_m/I_c) of NMIIB shows a highly significant reduction in cortical enrichment for the 1935D mutant, and a non-significant upward trend for the 1935A mutant, compared to wild-type GFP-NMIIB. **(G)** Accumulation during MPA over 250 seconds shows mechanoresponse for the 1935A mutant, while no significant accumulation is seen for the 1935D mutant or WT NMIIB. **(H)** Plotting peak mechanoresponse (I_p/I_o) and initial cortical enrichment (I_m/I_c) for each cell shows that all cells expressing the 1935D mutant are found in the lower right region of the graph (grey shaded area), while all cells expressing the 1935A mutant are found in the upper right region of the graph (unshaded region). Error bars are SEM, *p<0.05, **p<0.005, ***p<0.0005.

the I_p/I_o value at each time point to the I_p/I_o at t=0, then averaging each time point to create a single curve (**Fig. 3.4C**). While the 1935A mutant showed similar mechanoresponsiveness to wild-type NMIIB, the 1935D mutant showed much higher mechanoresponsiveness (**Fig. 3.4C**). Plotting each cell as a function of initial cortical enrichment (I_m/I_c) and peak mechanoresponse shows that all cells expressing NMIIB 1935A partition to the bottom right of the graph (shaded region) where most wild-type NMIIB cells are also found (**Fig. 3.4D**). In contrast, the 1935D-expressing cells are found in the upper left portion of the graph (unshaded region, **Fig. 3.4D**). Comparison of fluorescence intensity with mechanoresponse for the three NMIIB mutants shows very poor correlation (**Fig. 3.3B**). These data suggest that in HeLa cells, where a large fraction of NMIIB is associated with the cortex, reducing cortical association (1935D) improves mechanoresponsiveness.

To test whether increasing the cortical association of NMIIB would improve NMIIB mechanoresponsiveness in cells that have very low initial cortical association of NMIIB, we tested the same GFP-NMIIB phosphomimetic and non-phosphorylatable mutations in NIH 3T3s. Here, the 1935D mutant showed very low initial cortical association and no mechanoresponsiveness, while the 1935A mutant showed increased cortical association and mechanoresponsiveness over 5 minutes (**Fig. 3.4E, F, G**). Specifically, much like in HeLa cells, the 1935D mutant showed lower cortical enrichment than wild-type while the 1935A mutant showed a slight increase, although not a statistically significant change from wild-type (**Fig. 3.4F**). Plotting each cell as a function of initial cortical enrichment (I_m/I_c) and peak mechanoresponse shows that all cells expressing NMIIB 1935D partition to the bottom left of the graph (shaded region, **Fig. 3.4H**). In contrast, the 1935A-expressing cells are found in the upper right portion of the graph (unshaded region, **Fig. 3.4D**). Comparison of fluorescence intensity with mechanoresponse for the three NMIIB mutants shows very poor correlation (**Fig. 3.3C**). These data suggest that in NIH 3T3 cells, where a small fraction of NMIIB is associated with the cortex, increasing cortical association, even marginally, improves mechanoresponsiveness. The HeLa and NIH 3T3 cell graphs including the NMIIB tail mutants (**Fig. 3.4D, H**) appear to represent the right and left sides, respectively, of a biphasic relationship (**Fig. 3.2C,H**).

PKCζ expression and activity alters NMIIB cortical association and mechanoresponsiveness

To directly address the role of the kinase PKCζ in regulating the cortical association and mechanoresponsiveness of myosin II, we first measured the relative endogenous expression of the kinase in HeLa, Jurkat, and NIH 3T3 cells. NIH 3T3 cells showed the highest levels of PKCζ, followed by Jurkat and HeLa cells (**Fig. 3.5A**). Comparing mean cortical enrichment (I_m/I_c) values for NMIIA and NMIIB (**Fig. 3.2G**) to expression of PKCζ in the three cell types shows a steep negative correlation for NMIIB (**Fig. 3.5A**). The slope of the linear fit for NMIIB (-0.067) is more than five-fold steeper than the linear fit for NMIIA (-0.013). Due to the high expression of PKCζ and low cortical association of NMIIB in NIH 3T3 cells, we asked whether inhibition of PKCζ function, using a myristoylated-PKCζ pseudosubstrate inhibitory peptide (PKCζ inhibitor), would affect the cortical association of NMIIB. The addition of 10 µM PKCζ inhibitor significantly increased the cytoskeletal association of NMIIB, but not NMIIA, in NIH 3T3 cells (**Fig. 3.5B**). Treatment with the inhibitor also improved NMIIB mechanoresponsiveness, while NMIIA mechanoresponsiveness was unaffected (**Fig. 3.5C**). The magnitude of NMIIB mechanoresponsiveness seen in the presence of PKCζ inhibitor is very similar to that of the NMIIB 1935A mutant (**Fig. 3.4G**).

In HeLa cells, where NMIIB cytoskeletal association is high (**Fig. 3.2**) and PKCζ expression is low, we tested the effect of overexpression (OE) and activation of PKCζ on NMIIB cytoskeletal association and mechanoresponsiveness. Overexpression was performed transiently with either wild-type PKCζ or myristoylated-PKCζ, which is constitutively active due to anchorage on the plasma membrane. Compared with overexpression of an empty plasmid, NMIIA cytoskeletal association was not altered

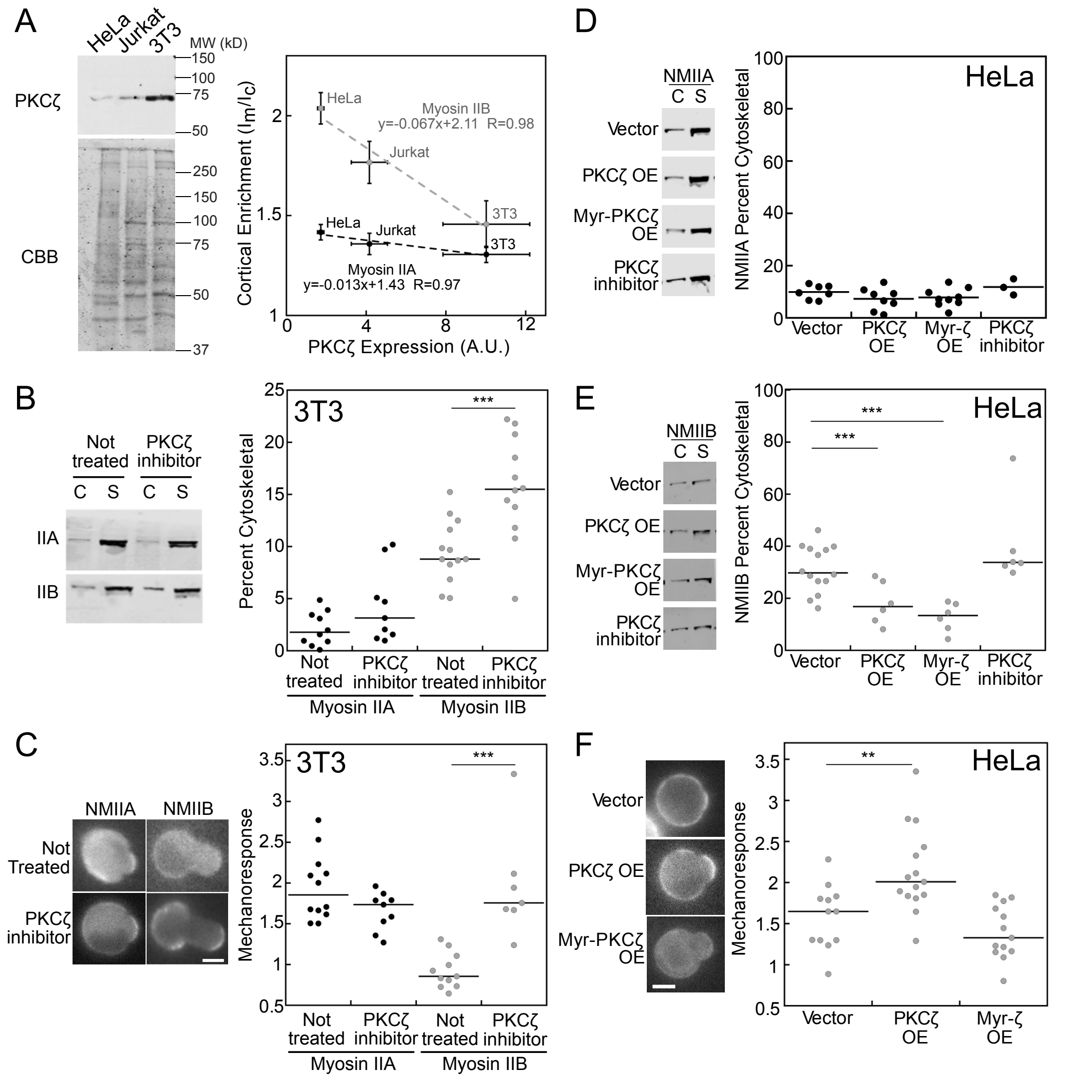

Figure 3.5. PKCζ expression and activity alters NMIIB cortical association and mechanoresponse. (A) PKCζ expression anti-correlates with NMII cortical enrichment, with 5-fold steeper slope for NMIIB than NMIIA. **(B)** PKCζ inhibition increases NMIIB cytoskeletal association and does not change NMIIA association in 3T3 cells. **(C)** Inhibition of PKCζ increases NMIIB mechanoresponse, but does not change NMIIA mechanoresponse in 3T3 cells. **(D)** Overexpression of PKCζ, constitutively active Myristoylated-PKCζ, or treatment with PKCζ inhibitor does not change NMIIA cytoskeletal association. **(E)** However, overexpression of PKCζ and Myr-PKCζ reduces the cytoskeletal association of NMIIB in HeLa cells, while PKCζ inhibitor has no effect. **(F)** PKCζ overexpression improves mechanoresponse, while Myr-PKCζ overexpression shows no change in mechanoresponse in HeLa cells. Error bars are SEM, *$p<0.05$, **$p<0.005$, ***$p<0.0005$.

upon PKCζ overexpression, myristoylated-PKCζ overexpression, or treatment with PKCζ inhibitor (**Fig. 3.5D**). However, NMIIB showed a significant reduction in the cytoskeletal fraction following 18-fold PKCζ and 10-fold myristoylated-PKCζ overexpression (**Fig.**

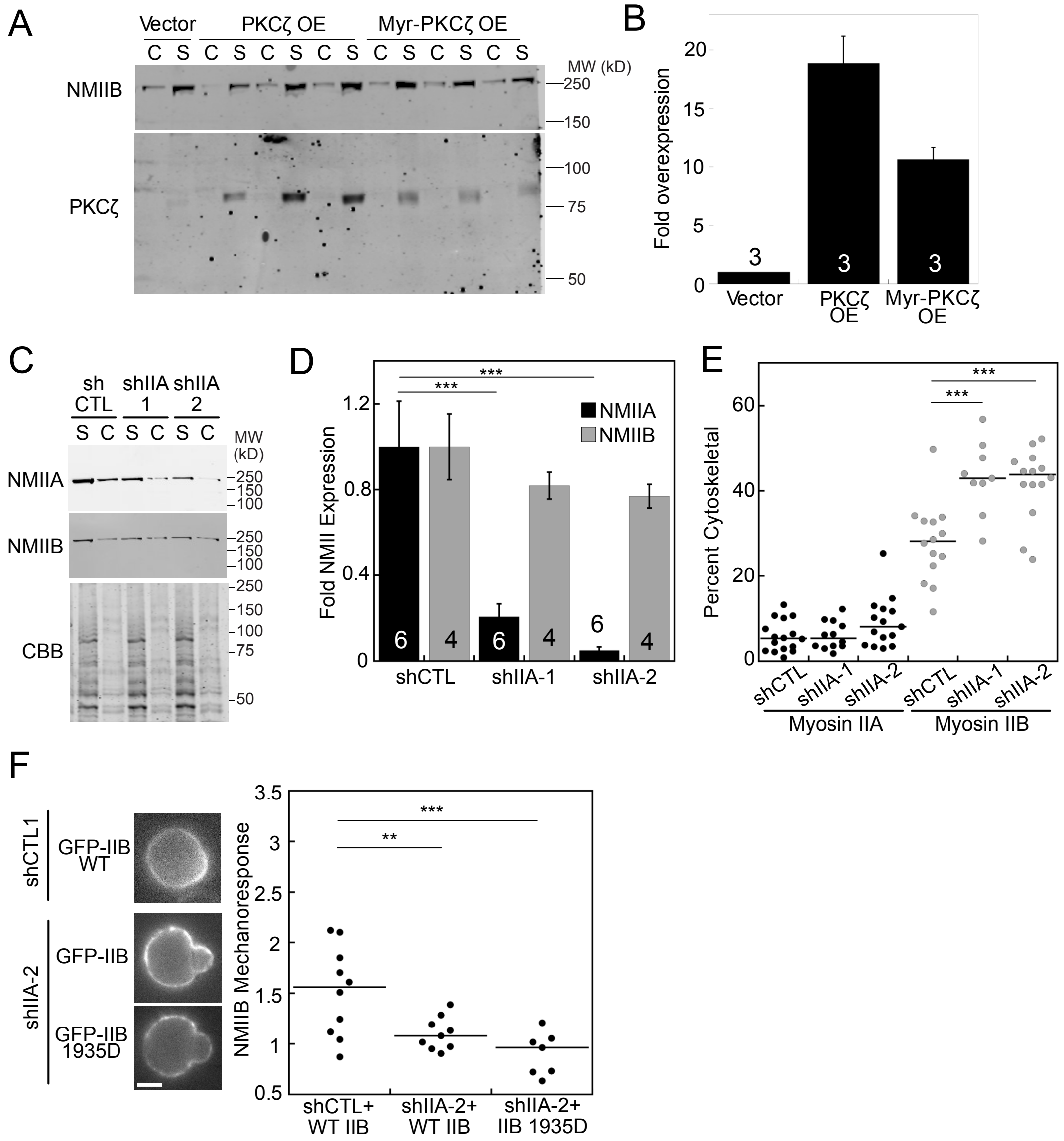

Figure 3.6. PKCζ overexpression and NMIIA knockdown alter mechanoresponse in HeLa cells. (A, B) The ratio of NMIIB in the cytoskeleton, C, to the supernatant, S, is altered by the overexpression of PKCζ or Myristoylated-PKCζ in HeLa cells. **(C, D)** NMIIA expression is significantly reduced in two HeLa shRNA NMIIA knockdown lines, while NMIIB expression does not significantly change. **(C, E)** In the two shRNA NMIIA knockdown lines, NMIIB cytoskeletal association is increased, while the association of the remaining NMIIA does not change. **(F)** GFP-NMIIB mechanoresponse is lost in the shIIA-2 knockdown line, and is not rescued by the NMIIB 1935D mutant. N-values displayed on bars, error bars are SEM, $*p<0.05$, $**p<0.005$, $***p<0.0005$.

3.5E; **Fig. 3.6A, B**). Inhibition of PKCζ did not significantly affect NMIIB cortical association (**Fig. 3.5E**), which is consistent with the finding that the NMIIB 1935A mutant behaves like wild-type NMIIB in HeLa cells (**Fig. 3.4B, C**). Interestingly, while the overexpression of wild-type PKCζ significantly increased NMIIB mechanoresponsiveness, the overexpression of myristoylated-PKCζ did not (**Fig. 3.5F**). This can be explained by the biphasic relationship between cortical association and mechanoresponsiveness: pushing NMIIB cytoskeletal association too low results in suboptimal mechanoresponsiveness.

We next sought to determine whether inputs to NMIIB assembly other than PKCζ could similarly perturb NMIIB mechanoresponsiveness. Due to the ability of NMIIA and NMIIB to co-assemble into hetero-filaments (92, 93), we reasoned that NMIIA could affect the filament assembly properties of NMIIB in cells. NMIIB assembly was indeed significantly higher in two HeLa NMIIA knockdown cell lines, compared to control (**Fig. 3.6C, E**). The percent NMIIA knockdown achieved in shIIA-1 and shIIA-2 was 80% and 95%, respectively (**Fig. 3.6D**). The large reduction in NMIIA expression in shIIA-2 is also accompanied by punctate distribution of GFP-NMIIB in the HeLa cortex (**Fig. 3.6F**), implying that NMIIA influences the dynamics of NMIIB assembly and turnover. This increase in assembly results in a reduction of mechanoresponsiveness (**Fig. 3.6F**), even with the NMIIB 1935D mutant, indicating that assembly-state is the primary determinant of NMIIB mechanoresponsiveness.

NMIIB mechanoresponsiveness depends on the fraction of free and assembled myosin II, not concentration of monomers

Since NMII accumulation is mediated by the addition of diffusing subunits to the mechanically loaded actomyosin network, we considered the possibility that the most sensitive parameter for mechanoresponsiveness was the concentration of free myosin in the cytosol. To measure total NMII concentration in cells, we compared endogenous NMIIA and NMIIB in HeLa cell lysates to known quantities of the purified tail fragment of NMIIA or NMIIB, which contains the antibody epitope (**Fig. 3.7A**). We then compared the amount of NMIIA and NMIIB in Jurkat and NIH 3T3 cells, loaded with equal amounts of total protein (**Fig. 3.7B**). This allowed for the calculation of the concentration of NMIIA and NMIIB in HeLa, Jurkat, and NIH 3T3 cells (**Fig. 3.7C**). To our knowledge, quantification of the concentration of NMIIA and NMIIB in mammalian cells has not been reported previously. The concentrations measured here, 200-550 nM NMIIA and 36-120 nM NMIIB, are similar to concentrations measured for the two myosin II isoforms in yeast (Myo2p: 450nM, Myp2p: 380nM, (94)), but lower than the 3.4 μM found in *Dictyostelium*

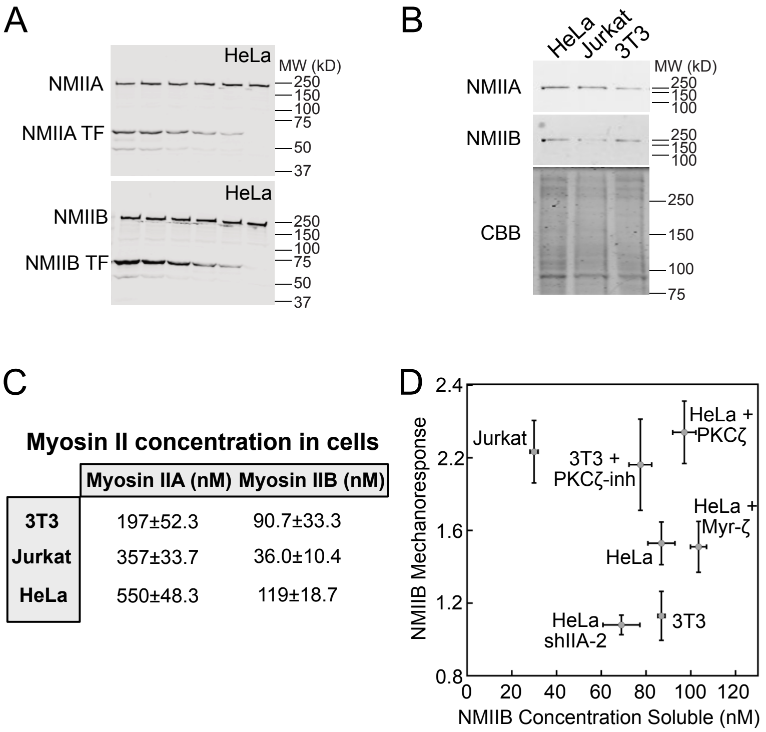

Myosin II concentration in cells

	Myosin IIA (nM)	Myosin IIB (nM)
3T3	197±52.3	90.7±33.3
Jurkat	357±33.7	36.0±10.4
HeLa	550±48.3	119±18.7

Figure 3.7. Concentration of monomeric NMIIB in cells does not predict mechanoresponse. **(A)** Quantification of NMIIA and NMIIB concentration in HeLa cells using a purified epitope standard. **(B)** Comparison of total-protein-matched 3T3 and Jurkat lysate to HeLa lysate allows **(C)** the quantification of NMIIA and NMIIB concentration in each cell type ± SEM. **(D)** Concentration of soluble NMIIB is not predictive of NMIIB mechanoresponse.

(95). A comparison of NMIIB mechanoresponsiveness and the concentration of soluble NMIIB (calculated from total NMIIB and the percent soluble, **Fig. 3.2B**) shows no obvious correlation (**Fig. 3.7D**). However, the comparison of the percent of NMIIB in the cytoskeletal fraction and NMIIB mechanoresponsiveness demonstrates a clear biphasic relationship (**Fig. 3.8A**). All conditions tested here are included in this graph, along with two additional cell lines (HEK 293 and Cos-7) which have been measured previously (49, 96). Overall, the ability of NMIIB to respond to mechanical stress is dependent on the ratio of cytoskeletal-associated and free NMIIB in a biphasic manner, with maximal mechanoresponsiveness occurring at a cytoskeletal association fraction of ~20%, very similar to what was observed in *Dictyostelium.*

An open question in the field of mechanobiology concerns the molecular mechanisms by which chemical and mechanical signals are integrated by cells. While molecular systems where mechanical inputs are sensed and converted into chemical signals have been studied, systems where chemical inputs tune the ability of molecular machinery to sense

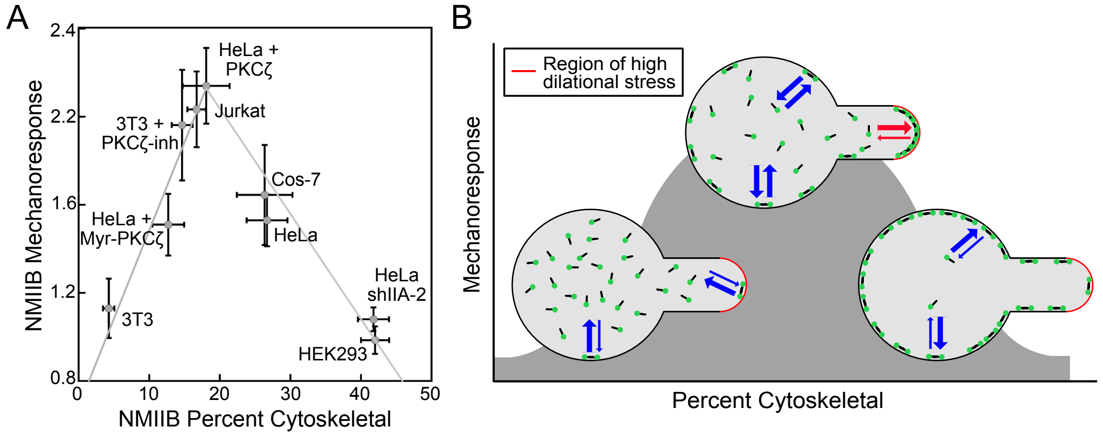

Figure 3.8. Relationship between NMIIB mechanoresponsiveness and cytoskeletal association is biphasic. (A) The fraction of NMIIB found in the cytoskeleton predicts NMIIB in a biphasic manner across many mammalian cell lines and conditions. **(B)** Graphical depiction of the relationship between cytoskeletal association and mechanoresponse. Low cytoskeletal enrichment reflects a relatively large amount of monomeric myosin with poor ability to assemble in response to stress. High cytoskeletal assembly reflects a relatively small pool of monomeric myosin, and an impaired ability to assemble new filaments at sites of stress. At an intermediate cytoskeletal assembly value, NMIIB mechanoresponse is maximal. Error bars are SEM.

and respond to forces are less well understood. We propose that in the case of myosin II, chemical signals, including phosphorylation through myosin heavy chain kinases like PKCζ, tune the setpoint for myosin II mechanoresponsiveness: enough myosin II must be assembled in the network to sense mechanical stress and lock-in the cooperative state while a sufficient free pool of subunits must be available to grow the actomyosin network in response to the mechanical stress (**Fig. 3.8B**). High levels of heavy-chain phosphorylation lead to low affinity for the bipolar filament and low levels of cytoskeletal association. Low levels of heavy-chain phosphorylation lead to high affinity for the bipolar filament and high levels of cytoskeletal association. An optimal condition exists where filament affinity is high enough to facilitate robust assembly locally at a site of stress, but low enough to allow for turnover in other regions of the cell to release free subunits. In fact, the mechanism by which NMIIB localizes to the rear of migrating cells is thought to be dependent on both mechanical and chemical signaling cues. Raab, et al*.* demonstrated that rear localization of NMIIB is mechanoresponsive; the occurrence of NMIIB polarization is dependent on substrate stiffness (65). On the other hand, Juanes-Garcia, et al*.* demonstrated that NMIIB localization is dependent on chemical signals driving phosphorylation of the heavy chain by PKCζ (58). The integration of these signals that allow for proper NMIIB localization and function can be explained by the mechanism outlined in this study: PKCζ tunes the setpoint of NMIIB assembly, which determines the ability of NMIIB to respond to mechanical stress.

CHAPTER 4. CONCLUSIONS

In this study, we have identified a number of actin cytoskeletal proteins that are able to accumulate to a site of imposed mechanical stress in the cell. By imposing a well-defined stress at a specific time using MPA, were able to quantify the kinetics of accumulation and geometries to which certain specific actin-binding proteins accumulate. These data provided mechanistic insight into mechanosensitive behaviors; some proteins display sigmoidal accumulation kinetics indicative of cooperative behavior while others do not, and some proteins accumulate to regions of the cell experiencing shear deformation, while other accumulate to regions experiencing dilation. We were able to validate, using agarose overlay, that global mechanical stress on cells also drives cortex association in these mechanoresponsive proteins. For both the actin-crosslinking proteins and myosin II, we observed biphasic behavior; a state exists where species respond optimally to external stress, while species with lower or higher affinity for binding the actin filament do not respond as well to this stress. For the actin crosslinking proteins α-actinin and filamin, the intrinsic actin-binding affinity of the paralog could be used to predict which paralog would be mechanoresponsive in our MPA assay, which closely mirrors the magnitude of stresses cells experience during cytokinesis and migration. These data can begin to explain mechanistically why some actin-crosslinking proteins accumulate to sites of stress in the cell, while others do not.

For α-actinin, we found evidence to suggest that a salt-bridge in the actin-binding domain plays a large role in mechanosensation by allowing the domain to switch between structural states having differing affinities for actin when force is applied. As the calponin-homology domain of α-actinin is highly conserved among many actin-binding proteins, this paradigm most likely extends to a number of actin-binding proteins, including utrophin, dystrophin, spectrins, and filamins. This notion, that a calponin-homology domain can sense tension on actin fibers, has been validated using the utrophin actin-binding domain in yet-unpublished work by Andrew Harris, PhD, in the laboratory of Daniel Fletcher, PhD, at University of California Berkeley.

In the case of myosin II, the assembly of myosin II into filaments with many actin-binding domains greatly influences its ability to remain associated with actin filaments due to its relatively low duty ratio compared with “walking” myosins. We demonstrate here that the kinetics by which myosin II assembles into filaments, which can be influenced by phosphorylation of the myosin II tail, has a biphasic impact on the ability of myosin II to accumulate in response to stress. This understanding of how chemical signaling events influence mechanical systems provides insight into how myosin IIB localization is determined in migrating cells, and more broadly, how the mechanical and chemical signals integrate in cells to generate predictable, force-dependent outcomes.

As growing evidence demonstrates that cell behavior is modulated by the mechanical properties of the actin network, the molecular mechanisms of the mechanoresponsive cytoskeletal elements involved become critical to understand. For example, mechanotransducing stress fibers, which dynamically form and dissolve during cell migration, are crosslinked largely by α-actinins and therefore could become more stable via α-actinin catch-bonding under load (97, 98). In addition to genetic diseases related to filamin B and α-actinin 4 mutations (99, 100), increased expression of the mechanosensitive paralogs of α-actinin and filamin are strong negative prognosticators in multiple metastatic cancers (101-103). As mentioned, the localization and behavior of myosin IIB in stress fibers during cell migration is known to depend on both chemical and mechanical inputs (58, 65). Defining the mechanisms by which individual proteins and the network as a whole respond to force and determining which cytoskeletal elements are mechanosensitive is essential for elucidating normal mechanosensitive biological processes and identifying new targets for inhibiting aberrant processes in disease states. In fact, the biphasic relationship between cortex affinity and mechanoresponse may be crucial to consider when designing treatment strategies for complex diseases, such as cancer. In some instances, it may be optimal to inhibit a process, but the same strategy may drive the system into a more aggressive, active state if the system is poised differently.

CHAPTER 5. FUTURE DIRECTIONS

In the future, I can envision many directions the study can take, but here I will discuss three specific lines of possible inquiry. The first involves investigation into the stress-sensing ability of the α-actinin actin-binding domain. The second involves characterizing the relationship between the expression of mechanoresponsive proteins and a cell's ability to migrate in physiologically-accurate scenarios. The third involves inquiry into how kinases which phosphorylate myosin themselves are regulated by mechanical stress.

To investigate the ability of the α-actinin actin-binding domain to sense stress, I envision both *in vivo* and *in vitro* approaches. The first step for an *in vitro* approach would be to purify the actin-binding domains of α-actinin 1, α-actinin 4, and α-actinin 4 with a K255E mutation labeled fluorescently. Using an optical trap or magnetic beads, tension would be placed on an actin filament, and the binding of the actin-binding domains monitored by an increase in fluorescence intensity. A next step would be to verify that the transition of the domain from a closed to an open configuration, due to breaking of the salt bridge at residue 255, is the mechanism by which the domain can sense stress. Mutating both of the residues involved in the salt bridge to cysteines would lock the protein in the closed configuration, and we would predict that *in vivo* (by MPA) and *in vitro* (by magnetic bead or optical trap) the domain would bind actin at relatively low affinity, but not be able to transition to the species that binds to actin under load at a higher affinity.

To begin an inquiry into how the expression of mechanoresponsive proteins alters cell migration, I would start with the highly-tunable myosin IIB in white blood cells, where migratory behavior is robust and which currently lacks endogenous myosin IIB. Preliminary data suggests that the expression of myosin IIB using adenovirus in mouse macrophages (RAW 264.7) increases their random migration velocity (data not shown).

In a next step, stable RAW 264.7 cell lines should be developed which express wild-type myosin IIB, the 1935A mutant, or the 1935D mutant. A careful quantification of the assembly state of these mutants should be done, followed by micropipette aspiration to determine the species which accumulates most robustly in response to applied stress. Random migration and chemotaxis assays can be done in 2D and 3D collagen matrixes to compare the contribution of the mutants of myosin IIB to migration speed in these different environments. Finally, the migration of macrophages expressing these variants of myosin IIB on different substrate stiffnesses could be compared to determine whether the different myosin phosphorylation states are tuned to respond to different substrate stiffnesses.

Third, it is known from data previously acquired by Tianzhi Luo, the *Dictyostelium* myosin heavy chain kinase C (MHCKC) accumulates in time with myosin II in response to MPA. In addition, altered activity of PKCζ has been shown to be stimulated by shear stress to cells using fluid flow. Thus, the question remains: How do kinases like MHCKC and PKCζ respond to stress and what effect does this have on myosin II? Normally, MHCKC is localized mostly to the cytoplasm, until cytokinesis or MPA. It is known that MHCKC does not localize properly to the cleavage furrow in the absence of myosin II, so it is likely that myosin II is required also for its localization in response to stress during MPA. Thus, can MHCKC sense the species of myosin II that is under stress? This would imply that some type of compliant element exists in the myosin II tail, where when the myosin II filament is stretched, MHCKC binding is increased. To test this, magnetic beads could be used to stretch a myosin II filament, and fluorescently-labeled MHCKC binding monitored. Fluorescent PKCζ would also be a great kinase to test in this experiment, with mammalian myosin IIB tails stretched by the magnetic beads. Ideally, kinase activity could be monitored during the assay, to determine whether the phosphorylation of the myosin II tail occurs primarily in the stressed or the unstressed condition.

CHAPTER 6. MATERIALS AND METHODS

Cell culture

Jurkat cells were cultured in RPMI 1640 (Sigma-Aldrich) with 10% FBS (Life Technology). HeLa, Cos-7, and NIH 3T3 cells were cultured in DMEM (Life Technology) with 10% FBS. For MPA experiments, adherent cells were cultured on tissue-culture treated dishes (Corning), detached using 0.05% trypsin (Life Technologies), centrifuged and resuspended in media. Transient transfections were performed using FuGene HD (Promega) for adherent cells, and electroporation for Jurkat cells. For FRAP studies, HeLa cells were cultured on glass-bottom dishes (Corning) and transferred to Leibowitz Media (Life Technology) + 10% FBS four hours prior to imaging.

Constructs

The following plasmids were acquired from Addgene:

Construct	Addgene Number	Resource
EGFP-C1-β-actin	31949	Vladislav Verkhusha
Mcherry-UtrCH-pCS2	26740	William Bement
mCherry-Ezrin-C14	55042	Michael Davidson
EGFP-C1-Talin	26724	Anna Huttenlocher
EFGP-N1-ACTN1	11908	Carol Otey
Mcherry-N1-coronin1B	27694	Christien Merrifield
E-cadherin-GFP	28009	Jennifer Stow
EGFP-C1-PH-PLCδ	21179	Tobias Meyer
mcherry-C1-cofilin	27687	Christien Merrifield
EGFP-MLCK-C2	46316	Anne Bresnick

pcDNA4-PKCZeta WT His	24609	Jeff Wrana
Myr.PKCzeta.FLAG	10802	Alex Toker

The Ras binding domain sequence from human Raf and the PH domain of human AKT were cloned into the FUW2 vector, tagged with GFP and mCherry respectively. GFP tagged constructs for EGFP-C3-myoIIA, EGFP-C3-myoIIB and EGFP-N3-myoIIC, were gifts from Robert Adelstein. CFP-C1-Kras, EYFP-C1-Rac1 and Lifeact-RFP-N1 were gifts from Takanari Inoue. EGFP-N1-ACTN4 was a gift from Allan Wells. A point mutation K255E was made in EGFP-N1-ACTN4 by site-directed mutagenesis to generate EGFP-N1-ACTN4 (K255E). The filamin A construct, pmdsRed-FLNA, was a gift from Fumihiko Nakamura. Filamin B full length construct EGFP-FLNB-pCI-C1, and hinge 1 deletion mutant construct EGFP-FLNB(ΔH1)-pCI-C1 were gifts from Arnoud Sonnenberg. Constructs for Septin 1 and 7, EGFP-N1-sept1 and EGFP-C1-sept7, were gifts from William Trimble. EYFP-paxillin and EGFP-vinculin were gifts from Susan Craig. GFP-tagged NMIIB containing 1935D and 1935A mutations were gifts from Miguel Vicente-Manzanares.

Drug treatment

Myosin II light chain inhibitor ML-7 (Sigma I2764) was dissolved in DMSO. The final concentration of DMSO in culture medium was kept below 0.15% during drug treatment. After resuspension, cells were treated with DMSO or ML-7 for 15 minutes prior to imaging. Myristoylated-PKCζ pseudosubstrate peptide inhibitor (Life Technologies) was dissolved in water and delivered to cells at 10 μM for one hour prior to imaging or cell lysis. Control cells received the carrier only.

Measurements of mechanosensory response of proteins using micropipette aspiration

Micropipette aspiration was performed as described previously (*28*). In short, a pressure difference was generated by adjusting the height of a motor-driven water manometer. Mammalian cells expressing desired fluorescent proteins were loaded into the observation chamber, which was filled with either DMEM or RPMI 1640 medium depending on the cell type. Cell types were deformed equally using the ratio of the aspirated length of the cell in the pipette (L_p) over the radius of the pipette (R_p) as a guide. Once a pressure was determined for each cell type for which L_p/R_p was approximately equal to two, this fixed pressure was used for all cells of that type. These values were different between cell types (0.075 nN/μm^2 for Jurkats, 0.15 nN/μm^2 for NIH 3T3s, 0.2 nN/μm^2 for HeLas, and 0.15 nN/μm^2 for Cos-7) due to the unique cortical tensions of these cells (**Fig. 2J**). Pressures higher than this often led to blebbing, or the separation of cell membrane from the cortex. All cells which demonstrated blebbing at any time during recording were discarded. Images were collected with an Olympus IX81 microscope equipped with Metamorph software and analyzed using ImageJ (National Institutes of Health). After background correction, the fluorescence intensity at the accumulation sites inside the micropipette were normalized against the opposite cortex of the cell. This was repeated for each frame to obtain timecourses and account for expression level variation and photobleaching.

Measurement of fluorescence recovery after photobleaching (FRAP)

FRAP was performed as described previously (22). HeLa cells were plated at low density on glass-bottom dishes and transiently transfected 40 hours prior to imaging. The culture media was changed to Leibowitz Media four hours prior to imaging. FRAP experiments were performed using a Zeiss AxioObserver with 780-Quasar confocal module, with a 63x (NA 1.4) objective at 37C and 5% CO_2. A small region of the cell cortex was bleached using a 488 nm Argon laser and the fluorescence recovery was recorded until recovery saturated (100 frames, 5-15 s/frame depending on the protein). The size and placement of the bleach region was kept relatively constant across measurements. For each frame, the average intensity of the bleached cortical region, reference (unbleached) region, and background was quantified using ImageJ (National Institutes of Health). For photobleaching correction, the reference theoretical intensity (RTI) was calculated by fitting the background subtracted reference intensity to an exponential decay equation as follows:

(1) $RTI(t) = A - B \cdot e^{-Ct}$

Where, A, B and C are fitting parameters.

The intensity of the bleached region was background subtracted and normalized to RTI. The normalized intensity (NI) was obtained by normalizing this to the pre-bleach intensity (average of 4 pre-bleach images), and was fitted to a single exponential as follows:

(2) $NI(t) = m_1(1 - m_2 \cdot e^{-kt})$

Where, m1, m2 are fitting parameters and k is the recovery rate.

The recovery time, τ, and the immobile fraction, F_i were measured as:

(3) Recovery time, $\tau = 1/k$

(4) Immobile fraction, $F_i = \frac{1-m_1}{1-m_1+m_2}$

Measurement of diffusion time by fluorescence correlation spectroscopy (FCS)

Jurkat (ACTN4) or HeLa (FLNB) cells were plated at low confluence in glass bottom dishes, transiently transfected 40 hours prior to imaging, and media was replaced with Leibowitz media 4 hours prior to imaging. FCS was performed exactly as previously described (22) at 37C and 5% CO_2 on a Zeiss AxioObserver with 780-Quasar confocal module & FCS, with a C-Apochromat 40x (NA 1.2) water objective.

Engineered cell lines

NMIIA knockdown lines were generated in HeLa cells using constructs from the Broad Institute TRC shRNA library distributed as bacterial glycerol stocks by Open Biosystems. The negative control construct (shCTL) was used, as well as:

HeLa shIIA-1 (TRCN0000029467): 5’-CCGCGAAGTCAGCTCCCTAAA-3’
HeLa shIIA-2 (TRCN0000029468): 5’-GCCAAGCTCAAGAACAAGCAT-3’

Target plasmids were co-transfected with generation 2.0 lentiviral packaging plasmids psPAX.2 (Addgene #12260) and pMD2.G (Addgene #12259), gifts from Didier Trono, via Transit 20/20 (Mirrus) transfection reagent into Lenti-X HEK293t cells (Clontech). Lenti-X HEK293t cells were allowed to produce virus for 48 hours, then media was collected and added to HeLa cultures. HeLa cells were treated with 5ug/mL puromycin (Life Technologies) until growth of resistant cells occurred. Knockdown was verified by western analysis.

Cytoskeletal fractionation

Adherent mammalian cells were trypsinized (Jurkat cells are non-adherent) and rotated in media for 10 minutes to allow for stress fibers to collapse, leaving behind primarily cortical actin cytoskeleton that had been allowed to equilibrate following loss of cell adhesion. This condition reflects the cytoskeletal organization probed by MPA when measuring mechanoresponse. All three cell types were then lysed using a buffer containing 50 mM PIPES pH 6.8, 46 mM NaCl, 2.5 mM EGTA, 1 mM ATP, 1 mM MgCl2, 0.5% Triton X-100, and a protease inhibitor cocktail containing benzamidine, leupeptin, pepstatin A, TPCK, TLCK, Aprotinin, and PMSF (osmotic strength was measured via conductance and found to be 17 mS/cm, equivalent to 150 mM NaCl).

Myosin quantification

Cells were trypsinized and counted, then centrifuged into pellets containing $5x10^5$ cells each. These pellets were washed in PBS and recentrifuged, then lysed in 75 µL RIPA lysis buffer plus 15 µL 6xSDS buffer. Due to cell volume and residual PBS, the total lysate volume reached 100 µL. 10 µL of lysate was added to each well of a 7% SDS-PAGE gel, or the equivalent of $5x10^4$ cells/well. In addition, each well was spiked with a known quantity of purified myosin II tail fragment, containing the epitope region for the antibodies used, with sequential 2-fold dilutions. A 7% gel was used because it allowed for optimal transfer of both the large molecular weight endogenous myosin II and the smaller molecular weight purified tail fragment out of the gel. Transfer was most effective at a constant 45V for 16 hrs, using PVDF membranes to prevent smaller protein pass-through and verifying complete transfer of larger proteins by performing a Coomassie stain to verify that no protein was left in the gel following transfer. The average volume of an individual cell for each cell type was determined from the micropipette aspiration images, where cell radius is measured, and assuming the cell shape to be a sphere prior to aspiration. For each experiment, a standard curve was created from the spiked tail fragment to determine the total number of moles of endogenous myosin II in each lane. The number of cells per lane multiplied by the average volume of a single cell gave the total cell volume per lane, and concentration was determined as a ratio of these two values.

Western analysis

SDS-PAGE gels with 10% acrylamide were made in house and transfers were performed at 90V for 90 minutes. Blots were blocked in 5% dry milk in PBS + 0.1% Tween-20 (Sigma) and incubated with primary antibodies overnight in 5% milk in PBS-T. The NMIIA antibody used was Poly19098 (BioLegend, 909801), the PKCζ antibody was H-1 (Santa Cruz, sc-17781), and the NMIIB antibody was from the Developmental Studies Hybridoma Bank, BF-F3, deposited by Schiaffino, S. (DSHB Hybridoma Product BF-F3). Blots were imaged using Li-Cor fluorescent secondary antibodies on the Li-Cor Odyssey CLx Blot Imager.

Model description for myosin II mechanoresponse

States considered

The computational model has been described previously (18, 41, 47). Briefly, we assume that monomers exist in one of four states: assembly-incompetent, unbound (to actin) monomers ($\overline{M}$); assembly-competent, unbound monomers (M); assembly-incompetent, actin-bound monomers ($\overline{M}^*$); and assembly-competent, actin-bound monomers (M^*). The latter is the fundamental unit of bipolar filament assembly. Two of these monomers bind to form parallel dimers (D^*) which then subsequently associate in an anti-parallel fashion to form the tetramer (T^*). Subsequently, dimers add laterally to the bipolar tetramer to build the bipolar filaments, which range in size from 3 to 36 dimers for *Dictyostelium* myosin II. The assembly scheme describing this process is illustrated in **Fig. 1.1C**, where the various interconversion parameters are given.

Interconversion between states

A full description of the interconversion between states has been described previously (41, 47) For the most part, interconversion between the various states is assumed to follow mass-action dynamics with constant rates. The exception is the rate constant k_{-1} which describes myosin unbinding to actin, and that this constant is force-dependent. In this case, we assume a Bell-like molecular catch bond model and compute:

$$k_{-1} = k_{-1}^{0}\mathrm{exp}(-\Delta E_b/k_bT)$$

where k_{-1}^{0} is the unbinding rate constant in the absence of force and cooperative interactions, and ΔE_b is the change in binding energy (E_b) associated with cooperative and force-dependent myosin II–actin binding. This is given by:

$$\Delta E_b = \Delta E_s + \frac{\mathrm{Force}}{\alpha\,\mathrm{myosin}}$$

where myosin is the total concentration of the bound myosin. The first term, ΔE_s, is the change in strain energy associated with myosin-actin cooperative interactions and is given by the piecewise linear function:

$$\Delta E_s = \begin{cases} \chi_1\phi, & \phi < \phi^* \\ \chi_1\phi^* + \chi_2(\phi - \phi^*), & \phi \geq \phi^* \end{cases}$$

where $\phi=3\times\mathrm{myosin}/C_{actin}$. The different nominal parameter values are given below (41, 47):

k_+	0.05	$s^{-1}\mu M^{-1}$	k_-	0.59	s^{-1}
k_{on}	0.45	$s^{-1}\mu M^{-1}$			
k_1	$k_{on}C_{actin}$	s^{-1}	k_{-10}	300	s^{-1}
k_2	0.37	$s^{-1}\mu M^{-1}$	k_{-2}	0.01	s^{-1}
k_3	0.0396	$s^{-1}\mu M^{-1}$	k_{-3}	0.0045	s^{-1}
k_4	1.25	$s^{-1}\mu M^{-1}$	k_{-4}	0.025	s^{-1}
k_n, $n>4$	2.50	$s^{-1}\mu M^{-1}$	k_{-n}, $n>4$	0.2	s^{-1}
χ_1	11.11	$k_B T$nm	χ_2	1.92	$k_B T$nm
α	36		$\phi*$	0.11	

Compartmental model

Spatially, we consider a compartmental model consisting of three compartments, one representing the cytosol and the other two cortical regions. The latter two represent the region of the cortex where aspiration pressure is applied from the remaining cortex. The cell is assumed to be a sphere of radius R_c=5 μm. The cortex forms a shell th=350 nm thick on the outside of this sphere. We assume that the aspirating pipette has a radius of R_p=2.5 μm and that the aspirated region forms a hemisphere of this radius. Thus, the total surface area of the cortex is $SA=4\pi R_c^2$ of which $SA_p=2\pi R_p^2$ experiences stress. Thus, the cytosol, cortex, aspirated cortex and unaspirated cortex compartments have volumes $V_{cytosol}=4\pi(R_c-th)^3/3$, $V_{cortex}=4\pi^3/3-V_{cytosol}$, $V_{cortex}(SA_p/SA)$ and $V_{cortex}(1-SA_p/SA)$ respectively.

Transfer between the different compartments is modeled by including a diffusive flux between the two cortical compartments and the cytosol. If D is the diffusion coefficient, then the flux per unit area is given by $-D\delta C/\delta x$ where C is the concentration of the species in question. For δx we use the thickness of the cortex. This is in units of numbers per unit area per time so we multiply by the surface area of the interface computed above. To account for the effect on the concentration of a molecule in a compartment we need to divide by that compartment's volume.

We assume that D=0.8 $\mu m^2/s$ is the diffusion coefficient of unbound myosin monomers, as measured in *Drosophila* S2 cells (104), which is very close to the diffusion coefficient for mCherry-myosin II measured for this study in *Dictyostelium* by Fluorescence Correlation Spectroscopy (0.97±0.35 $\mu m^2/s$). Bound monomers, dimers and tetrameters diffuse at 1/400 this rate. Bipolar filaments having more than three dimers do not diffuse.

Simulation implementation

The model was simulated by solving differential equations for each of the states (40 states) in each of the three different compartments (120 total states). Initial conditions for each of the states were first computed in the absence of any external stress. Thereafter, for each set of parameters, differential equations were solved using Matlab's (Mathworks, Natick, MA) ode23s stiff solver for 1000 seconds in the absence of force, followed by 300 seconds during which force $F=100k_bT$ was incorporated into the equation for k_{-1}.

Statistical analysis

Statistical analysis was performed with the using Graph Prism (www.graphpad.com) or KaleidaGraph (Synergy Software). The Mann-Whitney test was used for non-parametric comparisons of different data sets. Data sets were also analyzed by analysis of variance (ANOVA) with a Fisher's least significant difference comparison. Both methods obtained nearly identical conclusions.

CONTRIBUTIONS

Tianzhi Luo developed the initial framework for the characterization of mechanoresponsive proteins in mammalian cells. He and Xuyu Qian helped to quantify the mechanoresponse of many of the mechanoresponsive proteins in mammalian cells by MPA in the initial screening effort. Vasudha Srivastava identified the cell-cycle specific mechanoresponsive behavior of myosin IIB and characterized the ability of anillin to mechanorespond. Krithika Mohan developed the computational model describing the mechanoresponse of both actinin and filamin based on binding affinities. Yixin Ren performed the MPA studies on *Dictyostelium* myosin II, 3xASP, and 3xALA mutants. Pablo and Vicente Iglesias developed the computational model for myosin II mechanoresponse as it relates to filament assembly rates. Priyanka Kothari performed the FCS to determine diffusion times for myosin II. This work was supported by the NIH (GM66817 and GM109863) and DARPA (DARPA-BAA-16-17-BC-PA-015).

BIBLIOGRAPHY

1. Xu, K., G. Zhong, and X. Zhuang. 2013. Actin, spectrin, and associated proteins form a periodic cytoskeletal structure in axons. Science. 339: 452–456.

2. Nussenzveig, R.H., R.D. Christensen, J.T. Prchal, H.M. Yaish, and A.M. Agarwal. 2014. Novel α-spectrin mutation in trans with α-spectrin causing severe neonatal jaundice from hereditary spherocytosis. Neonatology. 106: 355–357.

3. Clark, A.G., K. Dierkes, and E.K. Paluch. 2013. Monitoring actin cortex thickness in live cells. Biophys. J. 105: 570–580.

4. Reichl, E.M., Y. Ren, M.K. Morphew, M. Delannoy, J.C. Effler, K.D. Girard, S. Divi, P.A. Iglesias, S.C. Kuo, and D.N. Robinson. 2008. Interactions between myosin and actin crosslinkers control cytokinesis contractility dynamics and mechanics. Current Biology. 18: 471–480.

5. Biro, M., Y. Romeo, S. Kroschwald, M. Bovellan, A. Boden, J. Tcherkezian, P.P. Roux, G. Charras, and E.K. Paluch. 2013. Cell cortex composition and homeostasis resolved by integrating proteomics and quantitative imaging. Cytoskeleton (Hoboken). 70: 741–754.

6. Podolski, J.L., and T.L. Steck. 1990. Length distribution of F-actin in Dictyostelium discoideum. Journal of Biological Chemistry. 265: 1312–1318.

7. Cano, M.L., D.A. Lauffenburger, and S.H. Zigmond. 1991. Kinetic analysis of F-actin depolymerization in polymorphonuclear leukocyte lysates indicates that chemoattractant stimulation increases actin filament number without altering the filament length distribution. J Cell Biol. 115: 677–687.

8. Meyer, R.K., and U. Aebi. 1990. Bundling of actin filaments by alpha-actinin depends on its molecular length. J Cell Biol. 110: 2013–2024.

9. Weihing, R.R. 1985. The filamins: properties and functions. Can. J. Biochem. Cell Biol. 63: 397–413.

10. Billington, N., A. Wang, J. Mao, R.S. Adelstein, and J.R. Sellers. 2013. Characterization of three full-length human nonmuscle myosin II paralogs. J. Biol. Chem. 288: 33398–33410.

11. Kollmannsberger, P., and B. Fabry. 2011. Linear and Nonlinear Rheology of Living Cells. Annual Review of Materials Research. 41: 75–97.

12. Guo, M., A.J. Ehrlicher, M.H. Jensen, M. Renz, J.R. Moore, R.D. Goldman, J. Lippincott-Schwartz, F.C. MacKintosh, and D.A. Weitz. 2014. Probing the stochastic, motor-driven properties of the cytoplasm using force spectrum microscopy. Cell. 158: 822–832.

13. Girard, K.D., C. Chaney, M. Delannoy, S.C. Kuo, and D.N. Robinson. 2004. Dynacortin contributes to cortical viscoelasticity and helps define the shape changes of cytokinesis. The EMBO Journal. 23: 1536–1546.

14. Girard, K.D., S.C. Kuo, and D.N. Robinson. 2006. Dictyostelium myosin II mechanochemistry promotes active behavior of the cortex on long time scales. Proceedings of the National Academy of Sciences. 103: 2103–2108.

15. Fabry, B., G.N. Maksym, J.P. Butler, M. Glogauer, D. Navajas, and J.J. Fredberg. 2001. Scaling the microrheology of living cells. Phys. Rev. Lett. 87: 148102.

16. Hoffman, B.D., G. Massiera, K.M. Van Citters, and J.C. Crocker. 2006. The consensus mechanics of cultured mammalian cells. Proceedings of the National Academy of Sciences. 103: 10259–10264.

17. Yang, L., J.C. Effler, B.L. Kutscher, S.E. Sullivan, D.N. Robinson, and P.A. Iglesias. 2008. Modeling cellular deformations using the level set formalism. BMC Syst Biol. 2: 68.

18. Luo, T., K. Mohan, P.A. Iglesias, and D.N. Robinson. 2013. Molecular mechanisms of cellular mechanosensing. Nat Mater. 12: 1064–1071.

19. Poirier, C.C., W.P. Ng, D.N. Robinson, and P.A. Iglesias. 2012. Deconvolution of the cellular force-generating subsystems that govern cytokinesis furrow ingression. PLoS Comput Biol. 8: e1002467.

20. Zhang, W., and D.N. Robinson. 2005. Balance of actively generated contractile and resistive forces controls cytokinesis dynamics. Proceedings of the National Academy of Sciences. 102: 7186–7191.

21. Roy, S., F. Miao, and H.J. Qi. 2010. Cell crawling assisted by contractile stress induced retraction. J Biomech Eng. 132: 061005.

22. Srivastava, V., and D.N. Robinson. 2015. Mechanical stress and network structure drive protein dynamics during cytokinesis. Curr. Biol. 25: 663–670.

23. Dai, J., H. Ping Ting-Beall, R.M. Hochmuth, M.P. Sheetz, and M.A. Titus. 1999. Myosin I Contributes to the Generation of Resting Cortical Tension. Biophys. J. 77: 1168–1176.

24. Kanada, M., A. Nagasaki, and T.Q.P. Uyeda. 2005. Adhesion-dependent and contractile ring-independent equatorial furrowing during cytokinesis in mammalian cells. Mol. Biol. Cell. 16: 3865–3872.

25. Ma, X., M. Kovács, M.A. Conti, A. Wang, Y. Zhang, J.R. Sellers, and R.S. Adelstein. 2012. Nonmuscle myosin II exerts tension but does not translocate actin in vertebrate cytokinesis. Proc. Natl. Acad. Sci. U.S.A. 109: 4509–4514.

26. Wang, Y.L. 1985. Exchange of actin subunits at the leading edge of living fibroblasts: possible role of treadmilling. J Cell Biol. 101: 597–602.

27. Theriot, J.A., and T.J. Mitchison. 1991. Actin microfilament dynamics in locomoting cells. Nature. 352: 126–131.

28. Mullins, R.D., J.A. Heuser, and T.D. Pollard. 1998. The interaction of Arp2/3 complex with actin: nucleation, high affinity pointed end capping, and formation of branching networks of filaments. Proceedings of the National Academy of Sciences. 95: 6181–6186.

29. Hung, W.-C., S.-H. Chen, C.D. Paul, K.M. Stroka, Y.-C. Lo, J.T. Yang, and K. Konstantopoulos. 2013. Distinct signaling mechanisms regulate migration in unconfined versus confined spaces. J Cell Biol. 202: 807–824.

30. Ibo, M., V. Srivastava, D.N. Robinson, and Z.R. Gagnon. 2016. Cell Blebbing in Confined Microfluidic Environments. PLoS ONE. 11: e0163866.

31. Petrie, R.J., H. Koo, and K.M. Yamada. 2014. Generation of compartmentalized pressure by a nuclear piston governs cell motility in a 3D matrix. Science. 345: 1062–1065.

32. van Haastert, P.J., and T.M. Konijn. 1982. Signal transduction in the cellular slime molds. Mol. Cell. Endocrinol. 26: 1–17.

33. Burgess, D.R., and F. Chang. 2005. Site selection for the cleavage furrow at cytokinesis. Trends in Cell Biology. 15: 156–162.

34. Chen, Q., G.S. Lakshmikanth, J.A. Spudich, and A. De Lozanne. 2007. The localization of inner centromeric protein (INCENP) at the cleavage furrow is dependent on Kif12 and involves interactions of the N terminus of INCENP with the actin cytoskeleton. Mol. Biol. Cell. 18: 3366–3374.

35. Hiramoto, Y. 1956. Cell division without mitotic apparatus in sea urchin eggs. Experimental Cell Research. 11: 630–636.

36. Dassow, von, G., K.J.C. Verbrugghe, A.L. Miller, J.R. Sider, and W.M. Bement. 2009. Action at a distance during cytokinesis. J Cell Biol. 187: 831–845.

37. Cabernard, C., K.E. Prehoda, and C.Q. Doe. 2010. A spindle-independent cleavage furrow positioning pathway. Nature. 467: 91–94.

38. Ou, G., N. Stuurman, M. D'Ambrosio, and R.D. Vale. 2010. Polarized myosin produces unequal-size daughters during asymmetric cell division. Science. 330: 677–680.

39. Kim, J.H., Y. Ren, W.P. Ng, S. Li, S. Son, Y.-S. Kee, S. Zhang, G. Zhang, D.A. Fletcher, D.N. Robinson, and E.H. Chen. 2015. Mechanical tension drives cell membrane fusion. Dev. Cell. 32: 561–573.

40. Ren, Y., J.C. Effler, M. Norstrom, T. Luo, R.A. Firtel, P.A. Iglesias, R.S. Rock, and D.N. Robinson. 2009. Mechanosensing through cooperative interactions between myosin II and the actin crosslinker cortexillin I. Curr. Biol. 19: 1421–1428.

41. Luo, T., K. Mohan, V. Srivastava, Y. Ren, P.A. Iglesias, and D.N. Robinson. 2012. Understanding the cooperative interaction between myosin II and actin cross-linkers mediated by actin filaments during mechanosensation. Biophys. J. 102: 238–247.

42. Kovács, M., K. Thirumurugan, P.J. Knight, and J.R. Sellers. 2007. Load-dependent mechanism of nonmuscle myosin 2. Proceedings of the National Academy of Sciences. 104: 9994–9999.

43. Tokuraku, K., R. Kurogi, R. Toya, and T.Q.P. Uyeda. 2009. Novel mode of cooperative binding between myosin and Mg2+ -actin filaments in the presence of low concentrations of ATP. Journal of Molecular Biology. 386: 149–162.

44. Uyeda, T.Q.P., Y. Iwadate, N. Umeki, A. Nagasaki, and S. Yumura. 2011. Stretching actin filaments within cells enhances their affinity for the myosin II motor domain. PLoS ONE. 6: e26200.

45. Orlova, A., and E.H. Egelman. 1997. Cooperative rigor binding of myosin to actin is a function of F-actin structure. Journal of Molecular Biology. 265: 469–474.

46. Kee, Y.-S., Y. Ren, D. Dorfman, M. Iijima, R. Firtel, P.A. Iglesias, and D.N. Robinson. 2012. A mechanosensory system governs myosin II accumulation in dividing cells. Mol. Biol. Cell. 23: 1510–1523.

47. Mohan, K., T. Luo, D.N. Robinson, and P.A. Iglesias. 2015. Cell shape regulation through mechanosensory feedback control. J R Soc Interface. 12: 20150512.

48. Buckley, C.D., J. Tan, K.L. Anderson, D. Hanein, N. Volkmann, W.I. Weis, W.J. Nelson, and A.R. Dunn. 2014. Cell adhesion. The minimal cadherin-catenin complex binds to actin filaments under force. Science. 346: 1254211–1254211.

49. Schiffhauer, E.S., T. Luo, K. Mohan, V. Srivastava, X. Qian, E.R. Griffis, P.A. Iglesias, and D.N. Robinson. 2016. Mechanoaccumulative Elements of the Mammalian Actin Cytoskeleton. Curr. Biol. 0: 1473–1479.

50. Ye, N., D. Verma, F. Meng, M.W. Davidson, K. Suffoletto, and S.Z. Hua. 2014. Direct observation of α-actinin tension and recruitment at focal adhesions during contact growth. Experimental Cell Research. : 1–11.

51. Ferrer, J.M., H. Lee, J. Chen, B. Pelz, F. Nakamura, R.D. Kamm, and M.J. Lang. 2008. Measuring molecular rupture forces between single actin filaments and actin-binding proteins. Proc. Natl. Acad. Sci. U.S.A. 105: 9221–9226.

52. Risca, V.I., E.B. Wang, O. Chaudhuri, J.J. Chia, P.L. Geissler, and D.A. Fletcher. 2012. Actin filament curvature biases branching direction. Proc. Natl. Acad. Sci. U.S.A. 109: 2913–2918.

53. Bieling, P., T.-D. Li, J. Weichsel, R. McGorty, P. Jreij, B. Huang, D.A. Fletcher, and R.D. Mullins. 2016. Force Feedback Controls Motor Activity and Mechanical Properties of Self-Assembling Branched Actin Networks. Cell. 164: 115–127.

54. Kikuchi, S., K. Honda, H. Tsuda, N. Hiraoka, I. Imoto, T. Kosuge, T. Umaki, K. Onozato, M. Shitashige, U. Yamaguchi, M. Ono, A. Tsuchida, T. Aoki, J. Inazawa, S. Hirohashi, and T. Yamada. 2008. Expression and Gene Amplification of Actinin-4 in Invasive Ductal Carcinoma of the Pancreas. Clinical Cancer Research. 14: 5348–5356.

55. Shibata, K., H. Sakai, Q. Huang, H. Kamata, Y. Chiba, M. Misawa, R. Ikebe, and M. Ikebe. 2015. Rac1 regulates myosin II phosphorylation through regulation of myosin light chain phosphatase. J. Cell. Physiol. 230: 1352–1364.

56. Vicente-Manzanares, M., X. Ma, R.S. Adelstein, and A.R. Horwitz. 2009. Cytoskeletal motors: Non-muscle myosin II takes centre stage in cell adhesion and migration. : 1–13.

57. Pasapera, A.M., S.V. Plotnikov, R.S. Fischer, L.B. Case, T.T. Egelhoff, and C.M. Waterman. 2015. Rac1-Dependent Phosphorylation and Focal Adhesion Recruitment of Myosin IIA Regulates Migration and Mechanosensing. Current Biology. 25: 175–186.

58. Juanes-García, A., J.R. Chapman, R. Aguilar-Cuenca, C. Delgado-Arevalo, J. Hodges, L.A. Whitmore, J. Shabanowitz, D.F. Hunt, A.R. Horwitz, and M. Vicente-Manzanares. 2015. A regulatory motif in nonmuscle myosin II-B regulates its role in migratory front-back polarity. J Cell Biol. 209: 23–32.

59. Brunello, E., M. Caremani, L. Melli, M. Linari, M. Fernandez-Martinez, T. Narayanan, M. Irving, G. Piazzesi, V. Lombardi, and M. Reconditi. 2014. The contributions of filaments and cross-bridges to sarcomere compliance in skeletal muscle. J. Physiol. (Lond.). 592: 3881–3899.

60. Ren, Y., H. West-Foyle, A. Surcel, C. Miller, and D.N. Robinson. 2014. Genetic suppression of a phosphomimic myosin II identifies system-level factors that promote myosin II cleavage furrow accumulation. Mol. Biol. Cell. 25: 4150–4165.

61. Geiger, B., J.P. Spatz, and A.D. Bershadsky. 2009. Environmental sensing through focal adhesions. Nat Rev Mol Cell Biol. 10: 21–33.

62. Johnson, C.P., H.-Y. Tang, C. Carag, D.W. Speicher, and D.E. Discher. 2007. Forced unfolding of proteins within cells. Science. 317: 663–666.

63. DuFort, C.C., M.J. Paszek, and V.M. Weaver. 2011. Balancing forces: architectural control of mechanotransduction. Nat Rev Mol Cell Biol. 12: 308–319.

64. Engler, A.J., S. Sen, H.L. Sweeney, and D.E. Discher. 2006. Matrix elasticity directs stem cell lineage specification. Cell. 126: 677–689.

65. Raab, M., J. Swift, P.C.D.P. Dingal, P. Shah, J.-W. Shin, and D.E. Discher. 2012. Crawling from soft to stiff matrix polarizes the cytoskeleton and phosphoregulates myosin-II heavy chain. J Cell Biol. 199: 669–683.

66. Chowdhury, F., S. Na, D. Li, Y.-C. Poh, T.S. Tanaka, F. Wang, and N. Wang. 2010. Material properties of the cell dictate stress-induced spreading and differentiation in embryonic stem cells. Nat Mater. 9: 82–88.

67. Ehrlicher, A.J., F. Nakamura, J.H. Hartwig, D.A. Weitz, and T.P. Stossel. 2011. Mechanical strain in actin networks regulates FilGAP and integrin binding to filamin A. Nature. 478: 260–263.

68. Effler, J.C., Y.-S. Kee, J.M. Berk, M.N. Tran, P.A. Iglesias, and D.N. Robinson. 2006. Mitosis-specific mechanosensing and contractile-protein redistribution control cell shape. Current Biology. 16: 1962–1967.

69. Thievessen, I., P.M. Thompson, S. Berlemont, K.M. Plevock, S.V. Plotnikov, A. Zemljic-Harpf, R.S. Ross, M.W. Davidson, G. Danuser, S.L. Campbell, and C.M. Waterman. 2013. Vinculin-actin interaction couples actin retrograde flow to focal adhesions, but is dispensable for focal adhesion growth. J Cell Biol. 202: 163–177.

70. Kee, Y.-S., and D.N. Robinson. 2013. Micropipette aspiration for studying cellular mechanosensory responses and mechanics. Methods Mol. Biol. 983: 367–382.

71. Discher, D.E., R. Winardi, P.O. Schischmanoff, M. Parra, J.G. Conboy, and N. Mohandas. 1995. Mechanochemistry of protein 4.1's spectrin-actin-binding domain: ternary complex interactions, membrane binding, network integration, structural strengthening. J Cell Biol. 130: 897–907.

72. Shin, J.-W., A. Buxboim, K.R. Spinler, J. Swift, D.A. Christian, C.A. Hunter, C. Léon, C. Gachet, P.C.D.P. Dingal, I.L. Ivanovska, F. Rehfeldt, J.A. Chasis, and D.E. Discher. 2014. Contractile forces sustain and polarize hematopoiesis from stem and progenitor cells. Cell Stem Cell. 14: 81–93.

73. Even-Ram, S., A.D. Doyle, M.A. Conti, K. Matsumoto, R.S. Adelstein, and K.M. Yamada. 2007. Myosin IIA regulates cell motility and actomyosin-microtubule crosstalk. Nature Cell Biology. 9: 299–309.

74. Vicente-Manzanares, M., M.A. Koach, L. Whitmore, M.L. Lamers, and A.F. Horwitz. 2008. Segregation and activation of myosin IIB creates a rear in migrating cells. J Cell Biol. 183: 543–554.

75. Roland, J., J. Berro, A. Michelot, L. Blanchoin, and J.-L. Martiel. 2008. Stochastic severing of actin filaments by actin depolymerizing factor/cofilin controls the emergence of a steady dynamical regime. Biophys. J. 94: 2082–2094.

76. Sutherland-Smith, A.J., C.A. Moores, F.L.M. Norwood, V. Hatch, R. Craig, J. Kendrick-Jones, and W. Lehman. 2003. An atomic model for actin binding by the

CH domains and spectrin-repeat modules of utrophin and dystrophin. Journal of Molecular Biology. 329: 15–33.

77. Weins, A., J.S. Schlondorff, F. Nakamura, B.M. Denker, J.H. Hartwig, T.P. Stossel, and M.R. Pollak. 2007. Disease-associated mutant alpha-actinin-4 reveals a mechanism for regulating its F-actin-binding affinity. Proceedings of the National Academy of Sciences. 104: 16080–16085.

78. Ehrlicher, A.J., R. Krishnan, M. Guo, C.M. Bidan, D.A. Weitz, and M.R. Pollak. 2015. Alpha-actinin binding kinetics modulate cellular dynamics and force generation. Proc. Natl. Acad. Sci. U.S.A. 112: 6619–6624.

79. Stossel, T.P., J. Condeelis, L. Cooley, J.H. Hartwig, A. Noegel, M. Schleicher, and S.S. Shapiro. 2001. Filamins as integrators of cell mechanics and signalling. Nat Rev Mol Cell Biol. 2: 138–145.

80. Shin, J.H., M.L. Gardel, L. Mahadevan, P. Matsudaira, and D.A. Weitz. 2004. Relating microstructure to rheology of a bundled and cross-linked F-actin network in vitro. Proceedings of the National Academy of Sciences. 101: 9636–9641.

81. Hird, S.N., and J.G. White. 1993. Cortical and cytoplasmic flow polarity in early embryonic cells of Caenorhabditis elegans. J Cell Biol. 121: 1343–1355.

82. Beach, J.R., G.S. Hussey, T.E. Miller, A. Chaudhury, P. Patel, J. Monslow, Q. Zheng, R.A. Keri, O. Reizes, A.R. Bresnick, P.H. Howe, and T.T. Egelhoff. 2011. Myosin II isoform switching mediates invasiveness after TGF-β-induced epithelial-mesenchymal transition. Proc. Natl. Acad. Sci. U.S.A. 108: 17991–17996.

83. Finer, J.T., R.M. Simmons, and J.A. Spudich. 1994. Single myosin molecule mechanics: piconewton forces and nanometre steps. Nature. 368: 113–119.

84. Even-Faitelson, L., and S. Ravid. 2006. PAK1 and aPKCzeta regulate myosin II-B phosphorylation: a novel signaling pathway regulating filament assembly. Mol. Biol. Cell. 17: 2869–2881.

85. Yumura, S., M. Yoshida, V. Betapudi, L.S. Licate, Y. Iwadate, A. Nagasaki, T.Q.P. Uyeda, and T.T. Egelhoff. 2005. Multiple myosin II heavy chain kinases: roles in filament assembly control and proper cytokinesis in Dictyostelium. Mol. Biol. Cell. 16: 4256–4266.

86. la Roche, De, M.A., J.L. Smith, V. Betapudi, T.T. Egelhoff, and G.P. Côté. 2002. Signaling pathways regulating Dictyostelium myosin II. J. Muscle Res. Cell. Motil. 23: 703–718.

87. Sabry, J.H., S.L. Moores, S. Ryan, J.H. Zang, and J.A. Spudich. 1997. Myosin heavy chain phosphorylation sites regulate myosin localization during cytokinesis in live cells. Mol. Biol. Cell. 8: 2605–2615.

88. Dulyaninova, N.G., and A.R. Bresnick. 2013. The heavy chain has its day: regulation of myosin-II assembly. Bioarchitecture. 3: 77–85.

89. Schiller, H.B., M.-R. Hermann, J. Polleux, T. Vignaud, S. Zanivan, C.C. Friedel, Z. Sun, A. Raducanu, K.-E. Gottschalk, M. Théry, M. Mann, and R. Fässler. 2013. β1- and αv-class integrins cooperate to regulate myosin II during rigidity sensing of fibronectin-based microenvironments. Nature Cell Biology. 15: 625–636.

90. Fernandez-Gonzalez, R., S. de M. Simoes, J.-C. Röper, S. Eaton, and J.A. Zallen. 2009. Myosin II dynamics are regulated by tension in intercalating cells. Dev. Cell. 17: 736–743.

91. Rai, V., and T.T. Egelhoff. 2011. Role of B regulatory subunits of protein phosphatase type 2A in myosin II assembly control in Dictyostelium discoideum. Eukaryotic Cell. 10: 604–610.

92. Beach, J.R., L. Shao, K. Remmert, D. Li, E. Betzig, and J.A. Hammer III. 2014. Nonmuscle Myosin II Isoforms Coassemble in Living Cells. Current Biology. 24: 1160–1166.

93. Shutova, M.S., W.A. Spessott, C.G. Giraudo, and T. Svitkina. 2014. Endogenous species of mammalian nonmuscle myosin IIA and IIB include activated monomers and heteropolymers. Curr. Biol. 24: 1958–1968.

94. Wu, J.-Q., and T.D. Pollard. 2005. Counting cytokinesis proteins globally and locally in fission yeast. Science. 310: 310–314.

95. Robinson, D.N., G. Cavet, H.M. Warrick, and J.A. Spudich. 2002. Quantitation of the distribution and flux of myosin-II during cytokinesis. BMC Cell Biol. 3: 4.

96. Surcel, A., W.P. Ng, H. West-Foyle, Q. Zhu, Y. Ren, L.B. Avery, A.K. Krenc, D.J. Meyers, R.S. Rock, R.A. Anders, C.L. Freel Meyers, and D.N. Robinson. 2015. Pharmacological activation of myosin II paralogs to correct cell mechanics defects. Proc. Natl. Acad. Sci. U.S.A. 112: 1428–1433.

97. Hotulainen, P., and P. Lappalainen. 2006. Stress fibers are generated by two distinct actin assembly mechanisms in motile cells. J Cell Biol. 173: 383–394.

98. Burridge, K., and E.S. Wittchen. 2013. The tension mounts: stress fibers as force-generating mechanotransducers. J Cell Biol. 200: 9–19.

99. Kaplan, J.M., S.H. Kim, K.N. North, H. Rennke, L.A. Correia, H.Q. Tong, B.J. Mathis, J.C. Rodríguez-Pérez, P.G. Allen, A.H. Beggs, and M.R. Pollak. 2000. Mutations in ACTN4, encoding alpha-actinin-4, cause familial focal segmental glomerulosclerosis. Nat. Genet. 24: 251–256.

100. Feng, Y., and C.A. Walsh. 2004. The many faces of filamin: a versatile molecular scaffold for cell motility and signalling. Nature Cell Biology. 6: 1034–1038.

101. Kikuchi, S., K. Honda, H. Tsuda, N. Hiraoka, I. Imoto, T. Kosuge, T. Umaki, K. Onozato, M. Shitashige, U. Yamaguchi, M. Ono, A. Tsuchida, T. Aoki, J. Inazawa, S. Hirohashi, and T. Yamada. 2008. Expression and Gene Amplification of Actinin-4 in Invasive Ductal Carcinoma of the Pancreas. Clinical Cancer Research. 14: 5348–5356.

102. Shao, H., S. Li, S.C. Watkins, and A. Wells. 2014. α-Actinin-4 Is Required for Amoeboid-type Invasiveness of Melanoma Cells. Journal of Biological Chemistry. 289: 32717–32728.

103. Iguchi, Y., S. Ishihara, Y. Uchida, K. Tajima, T. Mizutani, K. Kawabata, and H. Haga. 2015. Filamin B Enhances the Invasiveness of Cancer Cells into 3D Collagen Matrices. Cell Struct. Funct. 40: 61–67.

104. Uehara, R., G. Goshima, I. Mabuchi, R.D. Vale, J.A. Spudich, and E.R. Griffis. 2010. Determinants of myosin II cortical localization during cytokinesis. Curr. Biol. 20: 1080–1085.

ERIC SCHIFFHAUER

101 N. Wolfe Street, L01, Baltimore, Maryland 21231 | 301-471-4656 | eschiff1@jhmi.edu

EDUCATION

The Johns Hopkins University School of Medicine
PhD in Biochemistry, Cellular, and Molecular Biology. **October 2018**

George Mason University
BS Biology, *summa cum laude*, GPA 3.75 **May 2011**
Honors College member and Honors in Biology

RESEARCH EXPERIENCE

The Johns Hopkins University School of Medicine, Baltimore, Maryland
PhD Candidate **2013 – Present**
Non-muscle myosin II mechanoresponse in cell migration.
Principal Investigator: Dr. Douglas Robinson, PhD

The Johns Hopkins University School of Medicine, Baltimore, Maryland
Research Technologist **2011 – 2013**
Small-molecule impact on ion channel function in Cystic Fibrosis.
Principal Investigator: Dr. Pamela Zeitlin, MD PhD

National Center for Biodefense and Infectious Diseases, Manassas, Virginia
Undergraduate Apprentice and Student Researcher **2009 – 2011**
Role of pilin in the motility of model organisms of the biothreat pathogen
Francisella tularensis. Principal Investigator: Dr. Monique van Hoek, PhD

PROFESSIONAL EXPERIENCE

CordeRx, Inc., Baltimore, Maryland
Co-founder and Director of Operations **2017 – Present**
- Performed market analysis and competitive analysis, negotiated IP license terms,
and interfaced with key opinion leaders during the formation of a start-up company focused on providing a source of T-cells for liquid-tumor immunotherapies

Johns Hopkins Biotechnology Investment Group, Baltimore, Maryland
Executive Board Member **2017 – Present**
- Organized externship and stock pitch competition with T. Rowe Price, recruiting speakers from biotechnology investment, intellectual property, and clinical development backgrounds
- Performed market analysis, discounted cash flow valuation, and competitive analysis on biotechnology company for stock valuation report and pitch

Johns Hopkins Technology Ventures, Baltimore, Maryland
Commercialization Academy Analyst **2016 – 2018**

- Provided diligence on intellectual property, market, and licensing potential for more than 20 technologies developed by The Johns Hopkins University faculty

PUBLICATIONS IN PRESS (FIRST AUTHOR HIGHLIGHTED)

Duan R*, Kim JH*, Shilagardi K*, **Schiffhauer ES**, Son S, Lee D, Li S, Thomas C, Luo T, Fletcher DA, Robinson DN, Chen EH. Spectrin is mechanoresponsive protein shaping the architecture of the fusogenic synapse during cell-cell fusion. *Nat. Cell Biol.* In Press, 2018. (*authors contributed equally)

Schiffhauer ES, Robinson DN. Mechanochemical signaling drives cell shape change. *Biophysical Journal* 2017; 112: 207-214.

Kothari P, **Schiffhauer ES**, Robinson DN. Cytokinesis from nanometers to micrometers and microseconds to minutes. *Methods in Cell Biology* 2017; 137:307-322.

Schiffhauer ES*, Luo T*, Mohan K, Srivastava V, Qian X, Griffis E, Iglesias PA, Robinson DN. Mechanoaccumulative elements of the mammalian actin cytoskeleton. *Current Biology* 2016; 26(11): 1473-1479.

Miao C, **Schiffhauer ES**, Okeke EI, Robinson DN, Luo T. Parallel compression is a fast, low-cost assay for the high throughput screening of mechanosensory cytoskeletal proteins in cells. *ACS Applied Materials and Interfaces* 2017; 9(34): 28168–28179.

Lee S, Henderson MJ, **Schiffhauer ES**, Despanie J, Henry K, Kang PW, Walker D, McClure ML, Wilson L, Sorscher EJ, Zeitlin PL. Interference with ubiquitination in CFTR modifies stability of core glycosylated and cell surface pools. *Molecular Cell Biology* 2014; 34(14): 2554-65.

Schiffhauer ES, Vij N, Kovbasnjuk O, Kang PW, Walker D, Lee S, Zeitlin PL. Dual activation of CFTR and CLCN2 by lubiprostone in murine nasal epithelia. *AJP Lung Cell Molecular Physiology* 2013; 304(5): L324-31.

PUBLICATIONS IN PRE-PRINT OR REVIEW

Surcel A, **Schiffhauer ES**, Thomas DG, Zhu Q, DiNapoli K, Herbig M, Otto O, Guck J, Jaffee EM, Iglesias PA, Anders RA, Robinson DN. Harnessing the adaptive potential of mechanoresponsive proteins to overwhelm pancreatic cancer dissemination and invasion. *bioRxiv*; 2017; DOI: 10.1101/190553.

Mistriotis P, Wiskniewski E, Law RA, Bera K, Li Y, Tuntithavomwat S, Perez N, Afthinos A, Zhao R, Surcel A, **Schiffhauer ES**, Thomas DG, Robinson DN, Kalab P, Sun SX, Konstantopoulos K. Feeling the squeeze: How motile cells cope with different types of confinement. *In Review*, 2018.

Schiffhauer ES, Iglesias V, Ren Y, Iglesias PA, Robinson DN. Intrinsic myosin IIB mechanoresponse is tuned by paralog-specific heavy-chain phosphorylation. *In Review,* 2018.

RESEARCH PRESENTATIONS

Symposium Talk, Mechanobiology Subgroup – Biophysical Society National Meeting 2017

Platform Talk, Cell Mechanics, Mechanosensing, and Motility – Biophysical Society National Meeting 2015

Poster Presentations – American Society for Cell Biology National Meeting 2014, 2015, 2016, 2017

Poster Presentations – Biochemistry, Cellular, and Molecular Biology Program Retreat 2014, 2015

Poster Presentation – North American Cystic Fibrosis Conference 2012

Poster Presentation – American Society for Microbiology Biodefense and Emerging Disease Research Meeting 2010

AWARDS AND GRANTS

Isaac Morris Hay and Lucille Elizabeth Hay Graduate Fellowship	**2016 – 2017**
Johns Hopkins SOM Graduate Student Association Travel Grant	**2015**
Travel Grant to ASM Biodefense and Emerging Disease Research Meeting.	**2010**
Undergraduate Apprenticeship Program Grant	**2010 – 2011**
American Collegiate Rowing Association Second Team Academic All-American.	**2010 – 2011**
GMU Honors Program Academic Scholarship	**2007 – 2011**

SERIVICE AND OUTREACH

Thread, Baltimore, Maryland
Project Manager **2013 – Present**
Managed a team of mentors helping Baltimore City student raise his high school GPA, apply and be accepted to college, and navigate issues in his personal life

Summer Academic Research Experience, JHMI, Baltimore, Maryland
Instructor and Mentor **2014 – Present**
Mentored research projects and taught introductory math and biology coursework

George Mason University Honors College, Fairfax, Virginia
Elected Representative to Student Assembly Board **2009 – 2010**

PROFESSIONAL MEMBERSHIPS

American Society for Cell Biology, Biophysical Society, American Heart Association